University of Alberta

Characterization of Athabasca Asphaltenes Separated Physically and Chemically Using Small-Angle X-Ray Scattering

by

Jesús Leonardo Amundaraín Hurtado

A thesis submitted to the Faculty of Graduate Studies and Research
in partial fulfillment of the requirements for the degree of

Master of Science
in
Chemical Engineering
Department of Chemical and Materials Engineering

Fall 2010
Edmonton, Alberta

Examining Committee

Dr. John M. Shaw, Chemical and Materials Engineering

Dr. Greg Dechaine, Chemical and Materials Engineering

Dr. Hicham Fenniri, Chemistry

Abstract

Athabasca asphaltenes were characterized using small-angle X-ray scattering (SAXS) with synchrotron radiation. Two methods were used to separate asphaltenes from Athabasca bitumen. Conventional chemical separation by precipitation with n-pentane, and physical separation realized by passing bitumen through a zirconia membrane with a 20 nm average pore size. The Athabasca permeates and chemically separated samples were dispersed in 1-methylnaphtalene and n-dodecane, with temperature and asphaltene concentration ranges of 50-310 °C and 1-8 wt. %, respectively. Two approaches were also taken in the analysis of the SAXS emissions. A model-independent approach provided radii of gyration and scattering coefficients. A model-dependent fit provided size distributions for asphaltenes aggregates assuming that they are dense and spherical. Physically and chemically separated asphaltenes showed significant differences in nominal size and structure, and their structural properties exhibited different temperature dependencies. The results challenge the merits of using chemically separated asphaltene properties as a basis for asphaltene property prediction in crude oil/bitumen.

Acknowledgments

Through my path in life I have learned many things. At times, I have proven myself mistaken; and at times, I have enjoyed the taste of victory and satisfaction. Regardless of the outcome of my effort, I have realized that I need to assimilate all my experiences and extract something valuable out of them. I think that people underestimate the great value of defeat just because it does get you down; but after all that hurt is gone, one is left with very important lessons that make us grow professionally and most importantly, personally. Today, I want to take this opportunity to exercise my lesson of appreciating what success really is, happiness. As a human being, I have grown to be a humble person and accept that every little achievement that I have received is due to the help and collaboration of amazing people that I have had the pleasure to be surrounded with. Because I cannot pass on this opportunity without expressing my honest gratitude, I would like to explicitly say to the people that are important and that have made an impact in my life: thank you. Thank you for helping me succeed. Thank you for bringing happiness to my life!

First, I would like to thank Dr. John M. Shaw, my supervisor. Thank you for depositing all your trust in me with such an important project. Your vast knowledge, enthusiasm for research and constant encouragement were a definite inspiration for moving along in a project that we both know presented many challenges at first. It was very exciting to get to know someone that truly loves what he does, like you do. You also showed honest interest to know how I was doing in my life and if I ever needed someone to talk to, or seek advice from; I knew I could count on you. No other professor or supervisor has ever been that caring before and I really appreciate that. Thank you!

To my dearest friends: Keivan, Paola, Vanessa, Collins, Kasra, Ali, Inci, and Nayef. Thank you very much for all the support and help that you provided to me on a daily basis. We all know what it means to arrive in a different country and start building your support system from zero. Thank you for sharing this experience with me. It was great times and I honestly wish you all the success in the world in your professional careers that are now ahead of you! Enjoy it!

Thanks to the rest of the members from the Petroleum Thermodynamics Research Group, especially to Pat Ajas and Mildred Becerra. Thank you for being willing to help and assist me in whatever issue I had – most frequently related to US visa applications! Likewise, special acknowledgements to Bei Zhao and Martin Chodakowski for providing the samples and data that were used in this project.

I would like to acknowledge the funding provided by the sponsors of the NSERC Industrial Research Chair in Petroleum Thermodynamics: Natural Sciences and Engineering Research Council of Canada (NSERC), Alberta Innovates, Kellogg, Brown & Root (KBR) Energy and Chemicals, Halliburton Energy Services, Imperial Oil Resources, ConocoPhillips Canada Inc., Shell Canada Ltd., Nexen Inc., Virtual Materials Group (VMG), Total E&P Canada.

To my family, thank you for all your support and unconditional love. I strive to make you proud and I hope that you take this achievement to be yours as well. To all the members of my big family, especially those who are now gone, I thank you from the bottom of my heart for always reinforcing good values and morals in me. I love you all very much!

Finally, I would like to thank Kyle and the Boichat family for accepting and making me a part of their family. You have become a very important influence in my life and I am ever so grateful for all the great memories that we have shared together. Your constant encouragement and love have been a source of motivation to overcome hard times. No words can ever express the gratitude and love that I feel towards you. Because you truly make me feel at home and taken care of, I love you so much!

Thank you all!

Table of Contents

List of Tables

List of Figures

Nomenclature

$A_{lm}(q)$	Partial amplitudes from domain A
AB	Athabasca bitumen
AVR	Athabasca vacuum residue
A_S	Cross section of the beam
a	Sample-to-detector distance
B	Constant prefactor specific to the type of power-law scattering
CCD	Charged-coupled device
C_{lm}*	Partial amplitudes from domain B
D(R)	Size distribution
DLCA	Diffusion-limited cluster aggregation
$d\Sigma/d\Omega$	Differential scattering cross section per unit volume
$d\sigma/d\Omega$	Differential scattering cross section
F(q)	Coherent sum of scattering amplitudes of individual scattering centers
F(ω)	Angular envelope function
f(D)	Volume fraction distribution
f_{lm}	Shape coefficient
G	Exponential prefactor
g(r)	Pair correlation
I(q)	Normalized scattering intensity
I_a	Scattering intensity from domain A
I_b	Scattering intensity from domain B
I_e	Scattered intensity of an electron
I_o	Incident photon intensity per unit area per unit time
I_{0S}	Slit-smeared experimental scattering intensity

I_p	Primary intensity
I_S	Measured scattering intensity
I_T	Transmitted intensity per unit area per unit time
k	Packing factor
$\mathbf{k_i}$	Incident wave vector
$\mathbf{k_s}$	Scattered wave vector
l_0	Slit-height in reciprocal space
l_s	Sample thickness
N	Number of particles
N_b	Number of bins
N(D)	Number distribution
NMR	Nuclear magnetic resonance
N_T	Total number of scatterers
P	Scattering coefficient
P(q,r)	Form factor
q	Scattering vector, also denoted as Q
r	Radius
R_G	Radius of gyration
RLCA	Reaction-limited cluster aggregation
R_S	Radius of a sphere
S	Surface
S(q)	Structure factor
T_r	Sample transmission
V	Volume
V(D)	Volume distribution
$2V_N$	Volume of scatterers neglected

V_S	Volume of a sphere
W_y	Slight-width weighting function
W_z	Slit-height weighting function
W_λ	Wavelength weighting function
$Y_{lm}(\omega)$	Spherical harmonics
Z	Atomic number
$\gamma(r)$	Correlation function
Δ	Increment step for natural binning
ΔD_i	Width of bin *i*
$\Delta\rho$	Relative length density or contrast
$\Delta\Omega$	Solid angle between scattered photon and detector element
ε	Efficiency
ζ	Correlation distance
θ	Packing parameter for the hard sphere model
2θ	Scattering angle
λ	Wavelength
μ_l	Linear adsorption coefficient
ρ	Electron density
ρ_M	Electron density of the medium
$\Phi(qR)$	Scattering amplitude of a sphere
φ	Orientation angle
χ	Non-linear optimization parameter
$\psi(D)$	Probability of occurrence of a scatterer of dimension D

Chapter I
INTRODUCTION

1.1. Asphaltenes: The most enigmatic component of crude oil

Crude oils comprise a distribution of molecules with diverse chemical structures and molecular weights [1]. A self-assembling, high molar mass and polar fraction of crude oil, *asphaltenes*, are responsible for numerous complications during production, refining and transportation processes in the petroleum industry [1-4] and almost every operational stage of oil production is potentially at risk [5, 6]. The properties and stability of crude oil depends to a great extent on the behavior of asphaltenes. Changes in their interaction with the balance of crude constituents can cause asphaltenes to aggregate. Some factors that can induce deposition or precipitation of asphaltenic material are: compositional variation, chemical reaction and pressure variation [2, 7].

Asphaltenes are poorly defined on a molecular basis. Numerous operational definitions co-exist in the literature and are encountered in industry. The absence of clarity on this matter is a major stumbling block, as it leads to divergent perspectives on the relevant physics and chemistry associated with asphaltenes [8, 9]. This lack of clarity complicates the reading of the literature and is a critical limitation in the field. A better understanding of asphaltenes and their influence on the properties of reservoir fluids, bitumen and heavy oils, in particular, the focus of this work, would help resolve many of these problems [10]. A growing body of literature is targeting the definition of asphaltenes, and the behavior of asphaltenes from a molecular, thermodynamic, reaction, surface science, and aggregation perspective. A new field named, *Petroleomics* [11, 12], is beginning to develop.

1.2. Petroleomics

The most important liquid in the planet is what many call the source of life, *water*. The use and significance of water were recognized well before its structure was known. However, the discovery of its molecular structure allowed the scientific

community to understand and decipher its behavior. Though it is true that much about water is still to be understood, the knowledge of its molecular information brought answers to many mysteries that scientists did not comprehend before, such as its high boiling point and its ice density [12].

In medicine, it was not until Watson, Crick, Franklin, and Wilkins discovered the alphabet of human life in 1953, and it was read finally by 2003, that much was revealed about deceases and humans in general [12]. With the birth of *genomics*, the importance of structure was established, and numerous discoveries and advances have followed. Petroleomics is expected to have a similar impact in the petroleum sector as improvements in experimental techniques and theory accumulate. For now, ambiguity remains a major issue, as illustrated in the next section.

1.3. Molecular structure of asphaltenes

The reported average molecular weights of asphaltenes vary according to the experimental technique and source of asphaltenes used. Vapor pressure osmometry (VPO), a very popular colligative technique for the molecular weight determination of asphaltenes yields molecular weights with a broad range. Values greater than 100,000 g/mol were reported early on. More recent and careful experiments place values in the range 1500 - 4000 g/mol [13, 14]. However, the appropriateness of this method has been challenged [15-18]. The main problem with VPO is the required sample concentration. At approximately 1 wt. % it surpasses the critical nanoaggregate concentration (CNAC) of asphaltenes [16]. Assignments of molecular weights that correspond to aggregates is a key concern. Size exclusion chromatography (SEC) has also been applied, generating a bimodal molecular weight distribution of asphaltenes in the range of ~ 500-2000 g/mol [19]. Asphaltenes, however, are not miscible with the eluting solvent used during this study, 1-methyl-2-pyrrolidinone (NMP). As a result, soluble and insoluble asphaltene fractions are encountered [17]. Field-ionization mass spectroscopy (FIMS) and laser-desorption mass spectroscopy (LDMS) have also been applied, yielding average molecular weights for asphaltenes of 500-850 g/mol. However, molecular fragmentation and repeatability have led to concern the values obtained

[16, 17]. Fluorescence depolarization (FD) yields values of ~ 750 g/mol for petroleum asphaltenes. So, mean molar mass remains ambiguous.

As to average or notional molecular structure, both pericondensed structures [15-18, 20] characterized by a single polynuclear aromatic/naphthenic ring with multiple chains attached, and loose archipelago structures [13], characterized by multiple but small rings connected by alkane chains, have been proposed for asphaltenes, even for the same samples [13, 20, 21]. While chromophores are identified in some cases, proposed average molecule structures are typically constructed on the basis of NMR spectroscopy and Monte Carlo construction methods, which have also been challenged recently [22]. Support for archipelago structures is bolstered by agreement with pyrolysis, oxidation, and thermal degradation data [13]. However, the average or notional molecular structure of asphaltenes remains unresolved.

1.4. Aggregate structure of asphaltenes

The intention of petroleomics is to predict large-scale physical and chemical properties of petroleum fractions using molecular structure of components. For asphaltenes, there is no consensus on molecular definition. Thus, structure-function relationships must be based on the properties of asphaltene aggregates. As asphaltenes aggregate even at very low concentration, this may not prove to be a limitation in many practical or industrial applications where the characteristics of petroleum liquids may be driven by asphaltene aggregate properties [23].

The size of asphaltene aggregates has been reported to be as high as 1-2 μm using the time-of-transition method and confocal microscopy [24, 25]. On the other hand, spectroscopy techniques such as small-angle x-ray and neutron scattering (SAXS and SANS) have yielded aggregate sizes of 2-6 nm [3]. Much of this discrepancy is attributed to experimental differences in the method itself since the concentration range studied for these cases was similar. In fact, it is common to encounter very different results on asphaltene aggregate size depending on the method used.

On a different order of ideas, a hierarchy of the type of asphaltene component (core aggregates, medium aggregates, and fractal aggregates) has also been proposed depending on the size of the aggregate [26].

The physical structure and shape of aggregates are other unresolved and debated topics. For example, spheres, prolate ellipsoids, and oblate cylinders have been proposed [3, 27, 28]. Dense, loose, and fractal physical structures for asphaltene aggregates have been proposed based on experimental measurements [3, 29, 30]. Again, there is little agreement in the literature. This topic is addressed in greater detail in *Chapter II*.

1.5. Motivation

This research was designed to provide insights into the behavior of asphaltene aggregates using small-angle X-ray scattering (SAXS). The focus of this thesis is to analyze asphaltene size distribution and structure, of the physical properties of the aggregates and determine how these properties respond to changes in experimental conditions. More specifically, attention was paid to behavioral differences arising from differences in extraction methods. Nanofiltration, a physical separation method, and a standard solvent precipitation chemical separation method were applied to asphaltene separation. The results obtained in this study are expected to provide better comprehension of the phase behavior of asphaltene aggregates and hopefully, provide some insights concerning the relevance of chemical separation as a basis for understanding asphaltene aggregation in petroleum.

1.6. Thesis outline

The thesis comprises 7 chapters. Following this general introduction, the balance of the thesis comprises a literature review, general theory of SAXS, experimental and computational methodologies, results, and conclusions. A detailed review of the current literature on the topic of aggregate structure of asphaltenes is presented in *Chapter II*, along with a statement of the specific objectives of this research and closing remarks. *Chapter III* presents a summary of the theoretical aspects of small-angle scattering, with an emphasis on small-angle X-ray scattering. *Chapter IV* is devoted to explaining the choices of model independent and model dependent SAXS

data analysis methods. A description of the software used, as well as the equations, approximations and limitations involved in the analyses are also included. Experimental techniques and materials and the range of variables and experimental conditions are described briefly in *Chapter V.* Results are presented and discussed in *Chapter VI* along with implications regarding the behavior of asphaltenes and asphaltene aggregates. Conclusions and recommendations comprise *Chapter VII.*

Chapter II
LITERATURE REVIEW

2.1. Introduction

Current results from the scientific community regarding asphaltene properties, derived from small-angle scattering measurements, are reviewed in this chapter. The review focuses on pertinent aspects concerning asphaltene aggregate structure and size that lead to the specific objectives of this thesis.

2.2. Asphaltene aggregate structure and shape

The study of asphaltene aggregates constitutes a rather new area of investigation inside the petroleum field. Nonetheless, significant interest has been paid as multidisciplinary publications have been reported on them. In 1998, Fenistein *et al.* [5] reported on a series of viscosimetric and small-angle neutron scattering measurements on heptane-asphaltenes, identified as A and B, diluted in toluene/heptane mixtures with an asphaltenes volume fraction of 3 %. They found a constant scattering coefficient regardless of the toluene/heptane ratio and with a value of approximately 2 for both asphaltene samples, representative of open aggregates in solution that cannot be described by the conventional model of spherical micelles. They used this result along with intrinsic viscosity estimations to suggest a RLCA (reaction-limited cluster aggregation) or percolation aggregation mechanism based on the evidence of slow aggregation in the samples. In 2001, the same authors performed small-angle X-ray scattering measurements on ultracentrifuged heptane Safaniya asphaltenes in toluene, finding scattering coefficients similar to those obtained from their previous SANS measurements, favouring a RLCA aggregation mechanism [6]. In a different study, they performed small and ultra-small angle X-ray scattering (SAXS and USAXS) on three samples of filtered asphaltene powders [3]. Having a more ample q-range for study, they found that asphaltene aggregates can be very polydispersed materials ranging from 25 Å to over 1 μm. The scattering coefficient found for these samples was around 4, suggesting a rather compact structure with a smooth surface.

Gawrys *et al.* [4] presented their results from small-angle neutron scattering measurements on Arab Heavy, B6, Hondon, and Canadon Seco asphaltenes in heptane/toluene mixtures. The scattering coefficients ranged from ~ 1.7 (Arab Heavy asphaltenes) to 2.1 (Hondo asphaltenes), supporting the archipelago proposed structure for asphaltenes, where fused rings aromatic moieties are connected by aliphatic and heteroatomic groups. Adding resins to the asphaltene-heptol systems diminished the size of the aggregates while increasing the scattering coefficient to approximately 2.7, consistent with a dense packed aggregate of low porosity. Tanaka *et al.* [26, 31] performed SAXS, SANS, and X-ray diffraction measurements on Maya, Khafji, and Iranian Light heptane-asphaltenes using decalin, 1-methylnaphthalene, and quinoline as diluents. In SANS, the scattering coefficients for the Maya asphaltenes in decalin decreased from 2.7 to 2.4 while increasing the temperature from 25 °C to 350 °C. In SAXS, the behaviour was different as scattering coefficients dropped from ~ 4 to less than unity at 179 °C, 241 °C, and 243 °C for Khafji, Maya, and Iranian light asphaltene powders. When diluents were present, the scattering coefficients decreased from 3.95 to ~ 2 while increasing the temperature of the system. They also suggested that asphaltene aggregates undergo a structure transition from a large oblate ellipsoidal shape to a small spherical aggregate as temperature is raised. Other studies also concluded that asphaltenes may be constituted of loose and highly porous aggregates [24, 32, 33].

Headen *et al.* [34], carried out SANS and V-SANS measurements on asphaltene aggregates from two crude oils in solution with deuterated toluene. Using Beaucage functions, they were able to obtain values for radii of gyration along with scattering coefficients. In crude oils, asphaltene aggregates showed a scattering coefficient consistently higher than in toluene, indicating that asphaltene aggregates are denser in native oils. Increasing temperature resulted in a reduction of the aggregate size and structure order. With the assistance of very small-angle neutron scattering (V-SANS), the authors were able to obtain the low-q plateau in the emission profiles from which a radius of gyration of 0.45 μm was estimated. This served as clear evidence that asphaltenes are polydispersed, where different size groups seem to display different and almost independent behaviours. Barré *et al.* performed some viscosimetric and SAXS measurements on asphaltene fractions of reduced

polydispersity [35]. They obtained a scattering coefficient of 2.1 and tested two possible models that have been proposed for such value: the thin disk and fractal structure, concluding that better agreement was observed for the viscosity measurements with the fractal model. In concentrated samples (volume fractions > 0.15), the hard sphere model seemed to better described the viscosity results, but suggested that polydispersity as well as aggregate interactions should be taken into account for better modeling.

2.3. Asphaltene aggregate size

In 1995, Xu *et al.* completed some SAXS experiments on Athabasca asphaltenes in lights of achieving a characterization in regards of their size and shape [36]. They suggested that colloidal asphaltenes could not be properly described by a disc-like model, but by spherical particles instead. A calculation of the asphaltenes particle size volume-distribution was performed by fitting the general scattering equation with the sphere form factor through the method of least squares. The results showed bimodal distributions for asphaltenes in toluene, with the first distribution peak around 33 Å and the second one around 140 Å and 90 Å for asphaltene dispersions of 5 % and 15 %, respectively. Gawrys *et al.* [27], applied small-angle neutron scattering measurements on Arab Heavy, Canadon Seco and Hondon heptane-asphaltenes in order to deduce size and morphologies of the aggregates. Guinier analyses on heptane/toluene mixtures resulted in radii of gyration in the range of 40-70 Å; assessing the particle geometry that best describes the morphology of the asphaltenes aggregates in solution, they tested the monodispersed sphere, prolate cylinder, and oblate cylinder form factors. The oblate cylinder model provided the best agreement for the more intensely scattering samples; however, the chemical polydispersity of asphaltenes suggested that asphaltene aggregates should be polydispersed as well. Quality improvement was observed when Schultz distribution of particle radii was assumed at fixed particle length of ~ 20 Å, indicating that asphaltene aggregates are likely to be composed of polydispersed oblate cylinders.

Sheu presented results from extensive SAXS and SANS studies on Ratawi and Arabian Medium Heavy asphaltenes in toluene/pyridine mixtures and in their

vacuum residue state [23]. Regardless of the presence of diluents or not, the radii of gyration ranged from 25 Å to 45 Å and remained in the same range when the asphaltene concentration was increased too. Contrast variation analyses confirmed these results as valid and not a mere effect of the diluents presenting scattering contrast weakness. Similar results on radii of gyration for different asphaltene samples have been reported elsewhere [3, 5, 6, 11, 35].

A wide variety of methods has been applied to determine asphaltene aggregate size information. Evdokimov *et al.* employed near-UV/visible spectroscopy on Tatarstan heptane-asphaltenes in toluene solutions [37]. They concluded that at asphaltene concentrations below 1-2 mg/L monomers are the predominant species; in the concentration range 5-15 mg/L dimers are very stable, while at concentrations close to 90 mg/L dimers are paired forming nano-crystallites with estimated sizes of approximately 2 nm. Gradual build up of more complex asphaltene aggregates are formed afterwards. Da Silva and Rajagopal [38] determined the particle size distribution of Marlin asphaltenes in toluene/heptane mixtures by filtering the solutions through Millipore and Whatman filters with nominal sizes in the range 0.02-0.45 μm. They found that when diluted in toluene, asphaltene aggregates tend to accumulate in the smaller pore-size filters; whereas, as heptane is added in solution the aggregates tend to accumulate in the larger pore-size filters, especially in heptane/toluene solution ratios larger than 0.4, where most asphaltenes are retained in the 0.45 μm filter.

Bearsley *et al.* [39], applied confocal laser-scanning and fluorescence microscopy to Safaniya and San Joaquin asphaltenes in their native oils. They detected fluorescence in the 515-545 nm range that corresponds to particle sizes in the region of 2-7 μm; this result was confirmed by testing the fluorescence of maltene fractions which fluoresced significantly less. In a different study, Rastegari *et al.* employed a particle size analyzer based on the time-of-transition method to investigate the particle growth in model systems of Athabasca heptane-asphaltenes in heptane/toluene mixtures [24]. Individual asphaltene aggregates were found to be approximately 0.5-2 μm in diameter which tend to flocculate, up to 400 μm in size, into loose fractal-like flocs while increasing asphaltene concentration and

heptane content or decreasing the mixing rate. They estimated the asphaltene flocs to have a fractal dimension close to 1.6 as indication of their open structure.

Table 2.1. Summary of results from recent experimental works on asphaltenes

Study	Technique used	Asphaltene source	Diluent	Size (Å)	Structure	Shape
Barré et al. [35]	SAXS	Unknown	Toluene	60-160	---	Fractal, hard sphere
Bearsley et al. [39]	Confocal laser-scanning microscopy	Safaniya, San Joaquin	Native oils	2000-7000	---	---
Da Silva et al. [38]	Filtration	Marlim	Toluene + heptane	20 - >450	---	---
Evdokimov et al. [37]	Near-UV/ visible spectroscopy	Tatarstan	Toluene	~ 20	crystallite	Quasi-spherical
Fenistein et al. [5, 6]	SAXS SANS Viscometry	Safaniya	Toluene + heptane	60-200	Open	---
Gawrys et al. [4, 27, 40]	SANS	B6, Hondo, Arab Heavy, Gulf Coast, Canadon Seco	d-heptane + d-toluene	25-125	Varied surface roughness	Polydispersed oblate cylinders
Headen et al. [34]	SANS V-SANS	Unknown	Native oils	30-450	---	---
Maham et al. [33]	SAXS	Athabasca, Maya	n-dodecane, 1-MN	---	Loose	---
Rastegari et al. [24]	Particle-size analyzer	Athabasca	Toluene + heptane	500-2000	Loose	Sphere
Tanaka et al. [26, 31]	SANS X-ray diffraction	Maya, Khafji, Iranian Light	Decalin, quinoline, 1MN	100-30	Smooth surface fractal	Prolate ellipsoid & sphere
Savvidis et al. [3]	SAXS U-SAXS	Unknown	---	60-65	Compact, smooth	---
Sheu [11, 23]	SAXS SANS	Ratawi, Arab Medium Heavy	Native oils, toluene + heptane	25-45	---	---
Xu et al. [36]	SAXS	Athabasca	Toluene	33-140	---	Bimodal polydispersed spheres

2.4. Thesis objectives

As noted above in this chapter and summarized in Table 2.1, numerous aspects of the physical structure of asphaltene aggregates are not resolved. Contradictory results continue to be reported in the literature. The objectives of this thesis focus on providing insights into asphaltene aggregates linked to the limits and restrictions imposed by the experimental technique used. These are:

- Evaluate scatterer size distributions for physically and chemically separated asphaltenes using SAXS measurements.
- Compare and contrast asphaltene aggregate structures in diluents with divergent properties, n-dodecane and 1-methylnaphthalene.
- Determine the effect of temperature, concentration and type of solvent in the behaviour of asphaltenes, in respect of its structure, shape and particle size distribution.
- Benchmark the results obtained using light spectroscopy with results previously obtained through different techniques such as nanofiltration and acoustic spectroscopy.

Chapter III
SMALL-ANGLE X-RAY SCATTERING: Theory and Governing Equations

3.1. Introduction

This chapter presents the fundamentals of small-angle scattering (SAS) with special emphasis on small-angle X-ray scattering (SAXS). Details regarding the main equations and physical interpretation of the results are explained here. The chapter starts with a general description of small-angle scattering, followed by a description of the instrumentation required and data treatment and analysis techniques.

3.2. Small-angle scattering

Small-angle scattering (SAS) can be described as a fundamental method for structure analysis of condensed matter [41]. Applications cover experimental fields such as metal alloys, porous materials, biological macromolecules in solution, nanoparticles, emulsions, polymers, among others [41-45]. This method comprises small-angle scattering of X-rays (SAXS) and neutrons (SANS). Scattering occurs wherever electromagnetic radiation interacts with matter; and although the physical mechanisms of elastic X-ray and neutron scattering by matter are fundamentally different, they share the same mathematical formalism [42].

The development of small-angle scattering date from late 1930's with the seminal work from Guinier. However, it was not until the 1960's that the method was important to the scientific community as it allowed the extraction of low-resolution structural information on over all shape and internal structure in the absence of crystals. With the availability of synchrotron radiation and neutron sources in the 1970's, it was realized that this method could provide with minimal investment in time and effort, useful insights into the structure of non-crystalline biochemical systems [46].

Two of the main differences between SAXS and SANS are: neutrons are more sensitive to lighter atoms than X-rays; and there is a large difference between the neutron scattering lengths of hydrogen and deuterium. The latter presents an effective tool for selective labelling and contrast variation in neutron scattering by solvent exchange (H_2O/D_2O) or specific deuteration methods [41]. More details on SAXS and SANS are explained in the following sections.

3.2.1. Small-angle neutron scattering

Neutrons are scattered by nuclei, either by nuclear interactions with the atomic nucleus or magnetically, if the nucleus has a magnetic moment [42]. Since nuclei are significantly smaller than neutron wavelength, they act as point scatterers, and there is no angular dependence of the scattering of neutrons. However, neutron scattering is very difficult to predict since it depends on the nuclear mass, spin, energy levels, and on the nuclear isotopes that may be present [41]. Nuclei with spin have two scattering factors, one for spin-up state and one for spin-down state. Therefore, two types of neutron scattering are encountered, coherent scattering and incoherent scattering. Coherent elastic scattering results from the spatial distribution of nuclei within the particle; while incoherent scattering results from the interaction of random nuclear spin orientations with the spin of the incident neutrons. As can be expected incoherent neutron scattering exists only for nuclei with spin [42].

Neutron sources for small-angle scattering include *fission reactors* and *spallation* sources. In a nuclear reactor, the fission of U^{235} produces fast high-energy neutrons, which pass through a moderator such as H_2O or graphite at 300 K, where they reach thermal equilibrium after collision. Further enhancement of neutron wavelength is achieved with cold-source moderation and neutron guides. On the other hand, spallation neutron sources use proton accelerators to generate neutrons. The proton beam is accelerated through 500-800 MeV to strike a target made of uranium of tungsten. Each proton dislodges approximately 10-50 neutrons from the nucleus it hits. Spallation sources produce neutrons at very high intensities in 1-50 μsec pulses spaced 20-100 msec apart [42].

3.2.2. Small-angle X-ray scattering

X-rays are scattered by electrons. There are two components of scattering by X-rays; these are Thomson or coherent scattering, and Compton or incoherent scattering. The alternating electric field vector of the incident radiation imparts an alternating acceleration to the electron. Consequently, the electron becomes an oscillating charge which emits electromagnetic waves of the same wavelength λ, but phase-shifted by π. Even though the scattering occurs in all directions, it remains in the same phase. This is called coherent scattering [42]. Incoherent scattering is described as the elastic collision of an X-ray photon with an electron where both the energy and momentum are conserved, increasing the X-ray wavelength. Because incoherent scattering increases with the scattering angle, 2θ, it can be neglected during small-angle X-ray scattering [46].

3.3. Instrumentation for small-angle X-ray scattering

Essential components of an efficient SAXS instrument are a well collimated and monochromatic beam with sufficient photon flux, and detectors to measure the scattering intensity. The desired collimation can be obtained by a combination of focusing elements and slits. The optimum choice of these components and their combination depend on the source properties, desired beam characteristics, available detectors and other resources.

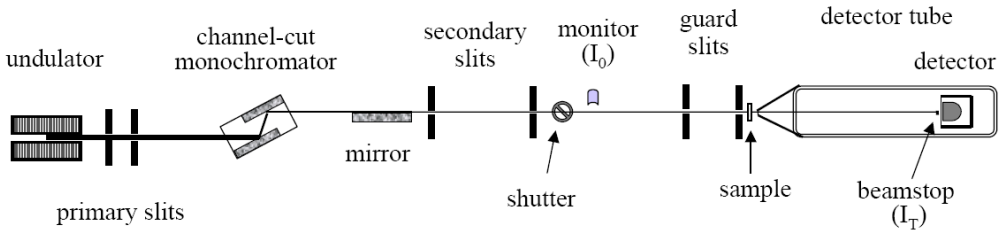

Figure 3.1. Schematic layout of a SAXS beamline at a synchrotron source [43]

Fig. 3.1 presents the typical configuration of a pinhole SAXS instrument at a synchrotron beamline. To avoid absorption and scattering by air, the entire path of the beam is under vacuum, except for the sample section. Parasitic background scattering is experimentally reduced with the presence of guard slits. Further details of the instrumentation are presented below.

3.3.1. Sources of X-rays

X-ray beams can be generated by *anode* or *synchrotron* sources. The first source involves a beam of high energy electrons striking an anode target (usually copper) in a vacuum. Part of the energy of the electrons is converted into X-rays and the rest into heat. The voltage at which the X-ray tube is run will determine the wavelength range of the X-ray spectrum and its intensity. For $Cu\ K_\alpha$ radiation (λ = 0.154 nm), an excitation voltage of 40 kV is frequently used [42].

In a synchrotron, the charged particles (electrons or positrons) orbit at relativistic speeds and the radiation is emitted when these relativistic particles are forced to a curved path. The storage ring consists of bending magnets which maintain electrons in closed orbits, and straight sections which accommodate the insertion devices consisting of periodic magnetic structures. The radiation emitted at the bending magnets is a powerful source of X-rays with a continuous spectrum. However, X-ray beams produced by the insertion devices are much more intense [43]. X-ray beams produced at a synchrotron source can be between 10 – 10^7 times more intense than those from anode sources [42].

The main advantages of a synchrotron radiation source over an anode source are: a) very high intensity; b) very good intrinsic collimation; c) the source is white; d) the radiation is plane-polarized; e) the radiation is emitted in pulses a few tenths of a nanosecond long with a repetition frequency of a megahertz [47].

3.3.2. X-ray optics and other instrumentation

In order to take advantage of the high brilliance of the source for a given application, the beam has to be conditioned by using the appropriate optical elements. The choice of optics should consider both the source properties as well as the detector at the end. The simplest element is the cooled primary slit which selects the central cone of the undulator beam, removing other stray radiations present. Since the full undulator harmonic is not sufficiently monochromatic, a crystal monochromator is used. This crystal should be able to withstand the high heat load resulting from the absorbed power of the full radiation. In reflection geometry, two or more reflections are used to reduce the parasitic tail of the reflection curve. Further conditioning of

the beam is provided by a focusing mirror which serves as an efficient cut-off filter of the higher harmonics reflected by the crystal monochromator [43].

The X-ray beam delivered from the advanced X-ray optics system is of very high quality. Therefore, a matching detector is required for a successful SAXS experiment. Options include gas-filled photon counting detectors, phosphor-based integrating detectors, and the more recently developed semiconductor-based pixel array detectors [42, 43, 47]. Gas-filled multiwire proportional chambers (MWPC) have served traditionally as SAXS detectors. This detector operates on the principle of gas ionization and has the advantage that electronic noise can be discriminated. It consists of a chamber filled with a high Z noble gas (*Ar* or *Xe*) and a polyatomic quenching gas. The incident radiation ionizes the gas and the electrons move towards the anode, where the location of the event is computed and histogrammed. However, its low count rate capability ($< 10^6$ counts/sec) and low spatial resolution (> 0.5 mm) cannot exploit the potential of a high-intensity X-ray beam [43].

In a phosphor-based integrating detector, the phosphor converts X-ray photons to visible photons which are detected (integrated) by a slow scan in a charge-coupled device (CCD). Here, a photocathode is placed behind the input phosphor that converts the emitted visible photons to photoelectrons which are then accelerated and electrostatically focused onto a smaller output phosphor that converts electrons back into visible photons. This electrostatic focusing and a large detecting area can be effectively coupled to the CCD. These detectors are not limited by count rate but by the charge capacity of the pixels (several hundred thousand electrons) and they provide good spatial resolution (< 100 μm) [43].

Pixel array detectors are based on thickly depleted semiconductors. In a semiconductor material, a given X-ray photon produces as many as an order of magnitude more electron-hole pairs than in gas. This, coupled with their high absorption makes them a very efficient detector. However, commercial use of these detectors is still on hold since a defect free readout structure still remains a major challenge [43].

3.4. General theory

For X-rays, the scattering originates from electrons and is nearly independent of λ, except in the close vicinity of the absorption edge of the constituent elements [41]. At small angles, the scattering is fully elastic because the energy of radiation is much higher compared to the typical excitations in the sample. Consequently, the magnitudes of the incident and scattered wave vectors are equal, $|\mathbf{k_i}| = |\mathbf{k_s}| = 2\pi/\lambda$ and the refractive index is close to unity [43]. The scattering vector is thus defined as, $\mathbf{q} = \mathbf{k_s} - \mathbf{k_i}$ and its magnitude:

$$q = |\mathbf{q}| = \frac{4\pi}{\lambda}\sin\theta \tag{3.1}$$

Using synchrotron radiation, the scattering vector can cover a wide range, 0.0006 Å^{-1} < q < 0.6 Å^{-1}, corresponding to real space dimension between 1 μm and 1 nm.

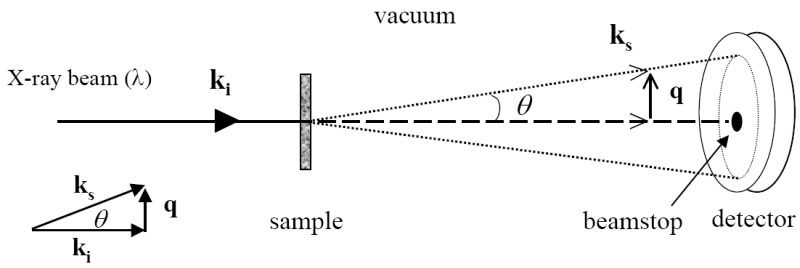

Figure 3.2. Schematic layout of a SAXS setup and definition of the scattering vector, **q** [43]

Two restrictions which are met in the majority of the cases, and which greatly simplify the problem are [47]:

a) The system is statistically isotropic. It makes no difference whether this is a property of the structure or a consequence of some change in time.
b) There exists no longer range order, meaning that there is no correlation between two points separated widely enough.

The intensity of X-rays scattered by an electron can be derived from the Maxwell's equations for the electromagnetic field emitted from an oscillating charged particle in the far field spherical wave approximation. The average scattered intensity is given by the magnitude of the time averaged Poynting vector (**S** = **E** x **H**) of the scattered field [47]:

$$I_e(\theta) = I_p \cdot 7.90\text{x}10^{-26} \cdot \frac{1}{a^2} \cdot \frac{1+\cos^2(2\theta)}{2} \tag{3.2}$$

where I_p is the primary intensity, and a is the sample-to-detector distance.

In the experiment depicted in Fig. 3.2, the incident photon intensity per unit area per unit time (I_0) is scattered by a sample and the scattered photons are acquired by each detector element subtending a solid angle, $\Delta\Omega$, with efficiency (ε). The measured intensity, considering negligible absorption, is given by

$$I_S = I_0 \cdot \varepsilon \cdot \Delta\Omega \cdot \frac{d\sigma}{d\Omega} \tag{3.3}$$

Since part of the incident radiation is absorbed along the beam path in the sample, the transmitted intensity per unit area per unit time is given by:

$$I_T = I_0 \cdot e^{-\mu_l \cdot l_s} \tag{3.4}$$

where μ_l is the linear absorption coefficient and l_s, is the sample thickness. The sample transmission is the ratio $T_r = I_T/I_0$. If $d\sigma/d\Omega$ per unit volume is incorporated to the equation, the following expression results:

$$I_S = I_0 \cdot \varepsilon \cdot T_r \cdot \Delta\Omega \cdot \mathrm{A_S} l_\mathrm{S} \cdot \frac{d\Sigma}{d\Omega} \tag{3.5}$$

where A_S is the cross section of the beam and $d\Sigma/d\Omega$ is the differential scattering cross section per unit volume, which contains information about the structure and the interactions in the system. To reach quantitative understanding of the measured intensity, a normalization of the data to $d\Sigma/d\Omega$ will be required. This will be denoted as $I(q)$.

For a dilute system containing N uniform particles per unit volume, the inter particle interactions can be neglected and $I(q)$ will mainly depend on the shape and size of the particles. Here, $F(q)$ represents the coherent sum of the scattering amplitudes of the individual scattering centers within the particle.

$$I(q) = N|F(q)|^2 \tag{3.6}$$

In small-angle scattering, the electron density can be approximated as a continuous function producing the following expression for the scattering amplitude:

$$F(q) = \int \rho(r)\, e^{iqr} dV \tag{3.7}$$

When the scattering centers are surrounded by a medium, such as a solvent, the relative length density or contrast ($\Delta\rho = \rho - \rho_M$) plays a relevant role in the scattering power,

$$F(q) = \int (\rho(r) - \rho_M)\, e^{iqr} dV \tag{3.8}$$

In the case of isotropic particles, the Fourier transform is reduced to the one-dimensional form:

$$F(q) = 4\pi \int_0^\infty \Delta\rho(r) \frac{\sin(qr)}{qr} r^2 dV \tag{3.9}$$

For randomly oriented particles, the intensity is isotropic in the azimuthal plane. For uniform spherical particle of radius R_S and volume V_S, equation (3.9) is transformed to:

$$|F(q)|^2 = V_S^2(\Delta\rho)^2 \left(\frac{3[\sin(qR_S) - qR_S\cos(qR_S)]}{(qR_S)^3}\right)^2 = V_S^2(\Delta\rho)^2 P(q, R_S) \tag{3.10}$$

$P(q,R_S)$ is the form factor for a sphere. Table 3.1 presents some form factors of frequently occurring shapes in small-angle scattering.

Table 3.1. Form factors of a few commonly observed shapes [43]

Shape	Formula
Uniform sphere of radius, R_S	$P(q, R_S) = \left(\frac{3[\sin(qR_S) - qR_S\cos(qR_S)]}{(qR_S)^3}\right)^2 = F_0^2(qRs)$
Randomly oriented cylinders of radius R_C and height H	$P(q, R_C, H) = \int_0^{\pi/2} \left\{\left[\frac{2J_1(qR_C\sin\varphi)}{qR_C\sin\varphi}\right]\left[\frac{\sin((qH/2)\cos\varphi)}{(qH/2)\cos\varphi}\right]\right\}^2 \sin\varphi\, d\varphi$ With φ = orientation angle
Spherical shell of inner and outer radii R_1 and R_2	$V^2P(q, R_1, R_2) = 16\pi^2[R_2^3F_0(qR_2) - R_1^3F_0(qR_1)]^2$
Spherical core-shell of core and shell radii R_1 and R_2	$F^2(q, R_1, R_2) = [V_2\Delta\rho_2F_0(qR_2) - V_1\Delta\rho_1F_0(qR_1)]^2$

For polydispersed scatterers, a size distribution, *D(R)*, with $\int D(R)dR = 1$ and a lower cutoff at *R=0*, are incorporated. However, the scattering function of a polydispersed system is determined by both the shape of the particles and its size distribution. It is impossible to determine the size distribution and the shape from a scattering experiment at the same time. Usually, it is assumed that the scattered intensity results from an ensemble of particles of the same assumed shape [47], leading to the following expression:

$$I(q) = N\Delta\rho^2 \int_0^\infty D(R)V^2(R)P(q,R)dR \tag{3.11}$$

The polydispersity is given by the ratio of the root mean square deviation of R_S (σ_S) and the mean value of R_S. Equation (3.11) can be numerically integrated using an experimentally determined size distribution or a theoretical distribution function [43].

When the scattering system is more concentrated, the scattering cross section involves an additional term that accounts for inter particle interactions, the structure factor [42-44, 46, 47]. This interference term, *S(q)*, is a complex function of *N* and the interaction potential. For dilute non-interacting particles, $S(q) \approx 1$. For spherical particles with a narrow size distribution, *I(q)* can be estimated by

$$I(q) = NV^2(\Delta\rho)^2P(q)S(q) \tag{3.12}$$

In the structure factor, the scattered intensity is correlated to the microstructure through a pair correlation, *g(r)*, which is the probability of finding a particle at a distance *r* from another particle.

$$S(q) = 1 + 4\pi\, N \int_0^\infty (g(r) - 1)\frac{\sin(qr)}{qr} r^2 dr \tag{3.13}$$

More complicated methods are used to account for structure factors for stronger particle interactions and wider size distributions [46, 47]. Guinier and Fournet [46], developed an approximation for the hard sphere model:

$$I(q) = const.\, \phi^2(qR)\frac{1}{1+\theta\phi(2qR)} \tag{3.14}$$

Where θ is the packing parameter, and $\Phi(qR)$ is the scattering amplitude of a sphere with radius R.

3.5. Data treatment and analysis

The radius of gyration, R_G, is defined as the mean square distance from the center of gravity, where the role of "mass" is played by electrons [47]. This concept is sound, regardless of the form of the particle. It is also the only precise parameter which can be determined by small-angle scattering experiments without using supplementary hypotheses [46].

Let us consider the amplitude of an oriented particle,

$$F(q) = \Delta\rho \int dV \cdot \cos(\boldsymbol{q}r) \tag{3.15}$$

By expanding $\cos(\boldsymbol{q}r)$ into a power series: $1 - \frac{(\boldsymbol{q}r)^2}{2} + \ \ldots$, the volume integral turns into $V\langle 1 - \frac{(qr)^2}{2} + \ \ldots\rangle$, where the average is taken keeping $\boldsymbol{q}$ fixed and varying r over the volume. In Cartesian coordinates, $\boldsymbol{q}r = \boldsymbol{q}(x\alpha + y\beta + z\gamma)$ and if the center of gravity is taken as the origin, $\langle(\boldsymbol{q}r)^2\rangle = q^2(x^2\alpha^2 + y^2\beta^2 + z^2\gamma^2)$.

$$I(q) = (\Delta\rho)^2V^2\langle 1 - q^2(x^2\alpha^2 + y^2\beta^2 + z^2\gamma^2) + \cdots\rangle \tag{3.16}$$

Knowing that $\langle\alpha^2\rangle = \langle\beta^2\rangle = \langle\gamma^2\rangle = 1/3$, and that $r^2 = x^2 + y^2 + z^2$, the Guinier approximation is established as:

$$I(q) = (\Delta\rho)^2V^2\left(1 - q^2\frac{R_G^2}{3}\right) \tag{3.17}$$

The higher order terms in Equation (3.16) are neglected since they depend on the special features of the particle [46]. Even with moderate anisometric particles Guinier's function will exceed the approximation. Size distributions will work in the same way [47]. However, this approximation is found to be valid only for $qR_G < 1$ [42-47].

If the shape of the particle is known or suspected *a priori*, the value of the radius of gyration can be used to extract the characteristic length of the particle. For more complex shapes, the radius of gyration provides another relationship between the

different characteristic lengths. Table 3.2 presents expressions for radii of gyration for some common shapes in small-angle scattering.

Table 3.2. Radii of gyration for simple bodies [42]

Shape	Formula
Sphere (radius r)	$R_G^2 = \frac{3}{5}r^2$
Hollow sphere (radii r_1, r_2)	$R_G^2 = \frac{3}{5}\cdot\frac{r_2^5 - r_1^5}{r_2^3 - r_1^3}$
Ellipsoid (semi-axes a, b, c)	$R_G^2 = \frac{a^2 + b^2 + c^2}{5}$
Prism with edge lengths A, B, C	$R_G^2 = \frac{A^2 + B^2 + C^2}{12}$
Elliptic cylinder (semi-axes a, b and height h)	$R_G^2 = \frac{a^2 + b^2}{4} + \frac{h^2}{12}$ $R_{XS}^2 = \frac{a^2 + b^2}{4}$
Hollow cylinder (radii r_1, r_2 and height h)	$R_G^2 = \frac{r_1^2 + r_2^2}{2} + \frac{h^2}{12}$ $R_{XS}^2 = \frac{r_1^2 + r_2^2}{2}$

In the asymptotic limit of the scattering curve, $qR_G \gg 1$, the scattering probes the interface of the particles. In the case of homogenous particles, $I(q) \propto q^{-4}$, which is known as the Porod behavior [43]. A more detailed explanation of Porod's law is presented in section 4.3.3.1. Nonetheless, this fourth power law has proved to perform equally well for single particles as for densely packed systems and for non-particulate structures, provided that they possess a well defined internal surface [47].

However, different power-law variations of *I(q)* have been obtained in SAXS from both compact and fractal morphologies [43]:

$$I(q) \propto q^{-p} \quad \begin{cases} p = 4 & \Rightarrow \textit{ sharp interface} \\ 3 \le p \le 4 & \Rightarrow \textit{ surface fractal} \\ 2 \le p \le 3 & \Rightarrow \textit{ mass fractal} \\ p \approx 2 & \Rightarrow \textit{ gaussian polymer chain} \\ p = 1 & \Rightarrow \textit{ thin randomly oriented filament} \end{cases} \tag{3.18}$$

This parameter, p, known as the scattering coefficient provides information about the internal structure of the particles. It can be inferred that the lower the scattering coefficient the lower the degree of structural order within the scatterers. Unstructured materials possess scattering coefficients of zero.

Other methods for SAS treatment include *Ab initio* analysis and *rigid body refinement* calculations. In an *Ab initio* method proposed by Stuhrmann [43], the particle shape is represented by an angular envelope function $r = F(\omega)$, describing the particle boundary in spherical coordinates *(r, ω).*

$$F(\omega) \approx F_L(\omega) = \sum_{l=0}^{L} \sum_{m=-l}^{l} f_{lm} Y_{lm}(\omega) \tag{3.19}$$

where f_{lm} are shape coefficients and $Y_{lm}(\omega)$ are spherical harmonics. The scattering intensity is calculated then by equation (3.21).

$$\rho_{C=} \begin{cases} 1, & 0 \le r < F(\omega) \\ 0, & r \ge F(\omega) \end{cases} \tag{3.20}$$

$$I(q) = 2\pi^2 \sum_{l=0}^{\infty} \sum_{m=-l}^{l} |A_{lm}(q)|^2 \tag{3.21}$$

$A_{lm}(q)$ are partial amplitudes computed from the shape coefficients f_{lm} using recurrent formulae based on 3j-Wigner coefficients. The following non-linear optimization expression is also employed:

$$\chi^2 = \frac{1}{N-1} \sum_{j=1}^{N} \left[\frac{I_{exp}(q_j) - \eta I(q_j)}{\sigma(q_j)} \right]^2 \tag{3.22}$$

In a *rigid body refinement* calculation, the particle is divided into domains. If the scatterer is divided in two domains, A and B, with known atomic structures, the scattering intensity is calculated by:

$$I(q, \alpha, \beta, \gamma, \boldsymbol{u}) = I_a(q) + I_b(q) + 4\pi^2 \sum_{l=0}^{\infty} \sum_{m=-l}^{l} Re[A_{lm}(q) C_{lm}^*(q)] \tag{3.23}$$

where $I_a(q)$ and $I_b(q)$ are the scattering intensities from domains A and B, respectively. $A_{lm}(q)$ are the partial amplitudes from domain A, while $C_{lm}^*(q)$ are those from domain B rotated by the Euler angles α, β, γ and translated by a vector $\boldsymbol{u}$.

3.6. Summary

Small-angle X-ray scattering is a very powerful technique for structural studies in condensed or semi-condensed matter. In this chapter, both experimental and theoretical details about SAXS were presented. Modern tendency towards using sophisticated mathematical methods such as *Ab initio* or rigid body refinement analyses gives small-angle scattering a wider application spectrum. However, when minimal information is known about the scattering system numerous assumptions have to be made in order to extract the required structural information. Statistical and model-independent size information can be acquired from the radius of gyration, R_G. For power-law scattering, the scattering coefficient also supplies insights about the morphology and internal structure of the scatterers. In spite of this, scattering coefficients are also subject to multiple interpretations. In the case of polydispersed mixtures it is not feasible to obtain shape and particle size distribution at the same time. The practical approach involves the assumption of the most probable particle shape.

Chapter IV
COMPUTATIONAL APPROACH

4.1. Introduction

Details on the analysis of the data are presented in this chapter. Application of analytical solutions to small-angle scattering experimental data is a very difficult, time-consuming, and for many cases unfeasible. Numerical and approximate solutions have been implemented. These latter approaches, implemented in commercial software were selected for this work. The chapter is divided in two sections. The first one, dedicated to the visualization of the CCD images; and the second one, to the analysis of the SAXS spectra where particulars about the software used as well as the mathematical methods chosen for this study are described.

4.2. Data visualization

Scanning Probe Image Processor, SPIP™ version 4.8 was selected for visualization [48]. Experimental emission images were obtained from a charge coupled device (CCD) detector during the SAXS experiments. The CCD detector possessed very high resolution, resulting in 3000 x 3000 pixel images. Each image was imported using the *heuristic file importer* tool. Required information to import the images included the number of X and Y pixels (3000 x 3000), and the header length of the files which was 5632 bytes. The data was imported using a 16 bit integer format.

Fig. 4.1 shows an example image. The center point corresponds to the protective beam stop of the CCD detector. Adjacent to the beam stop, one observes gradients of color representing the intensity of the scattered photons. The scattering intensity is in the order presented in the color bar. Scattering angle increases with distance from the beam stop. Black areas in the image correspond to dead pixels that are averaged out during the extraction of intensity profiles.

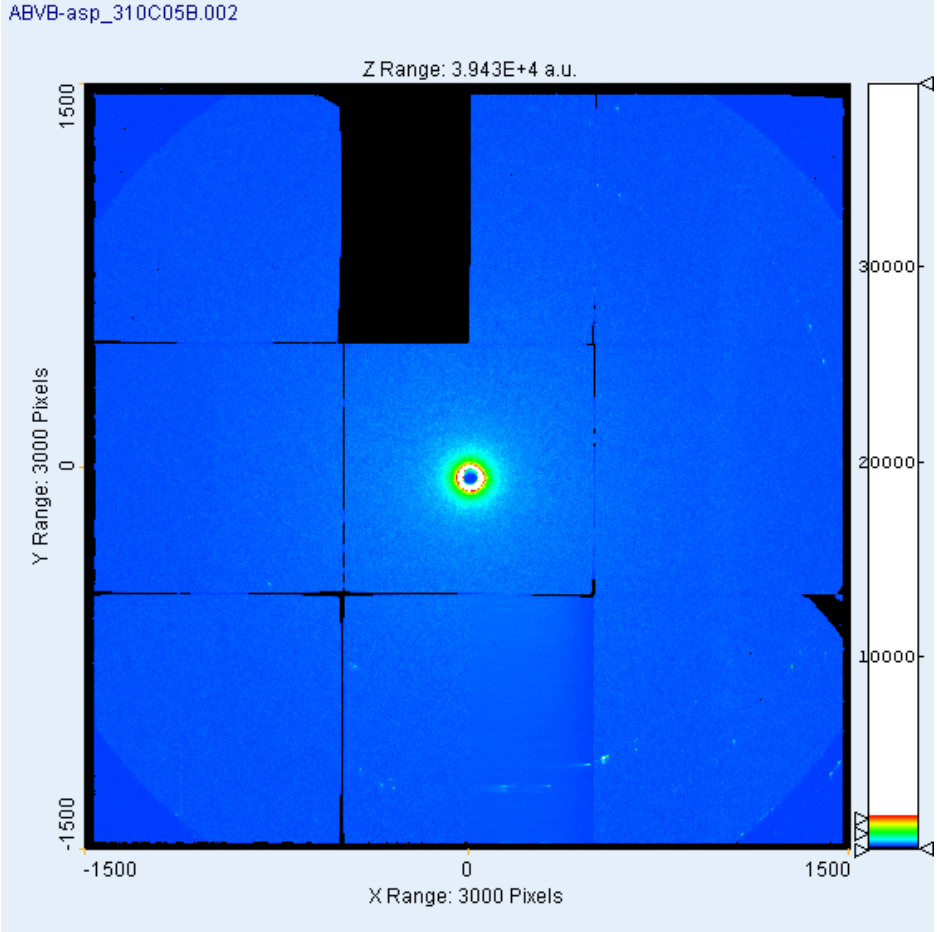

Figure 4.1. CCD image for 1 wt. % AVR-asphaltenes in n-dodecane at 310 °C (exposure time: 0.02 s)

4.3. Data processing

In this section, details regarding data processing are addressed. The software used, as well as initial treatment of the data, and methods chosen for the estimation of the aggregate particle size and asphaltene structural information are also described.

4.3.1. Software

IGOR Pro version 6.0, was used as the main platform for data analysis [49]. This integrated program can be used for visualizing, analyzing, transforming, and presenting data. It was originally designed to deal with waveform data, which consists of hundreds of thousands of values measured at evenly spaced intervals. Also, Igor procedures permit customized data processing.

In this work, *Irena SAS modeling macros* version 2.27 was implemented as an Igor procedure [50, 51]. This package was designed at the Advanced Photon Source in the Argonne National Laboratories to evaluate small-angle scattering (SAS) data. Some applications already built in include: Guinier, Porod, Kratky, and Zimm plots; particle size distribution estimation; unified exponential/power-law model; reflectivity methods, among others.

4.3.2. Initial data treatment

4.3.2.1. Background subtraction

The intensity profiles were loaded into Igor using the *data import* tool. The columns for *q*, *I(q)*, and *error* were saved as separate waves in a QRS folder. The units for *q* were selected as Å^{-1}. The effect of background scattering during the experiments was evaluated using SAXS emissions for air, an empty tube, and different solvents in tubes.

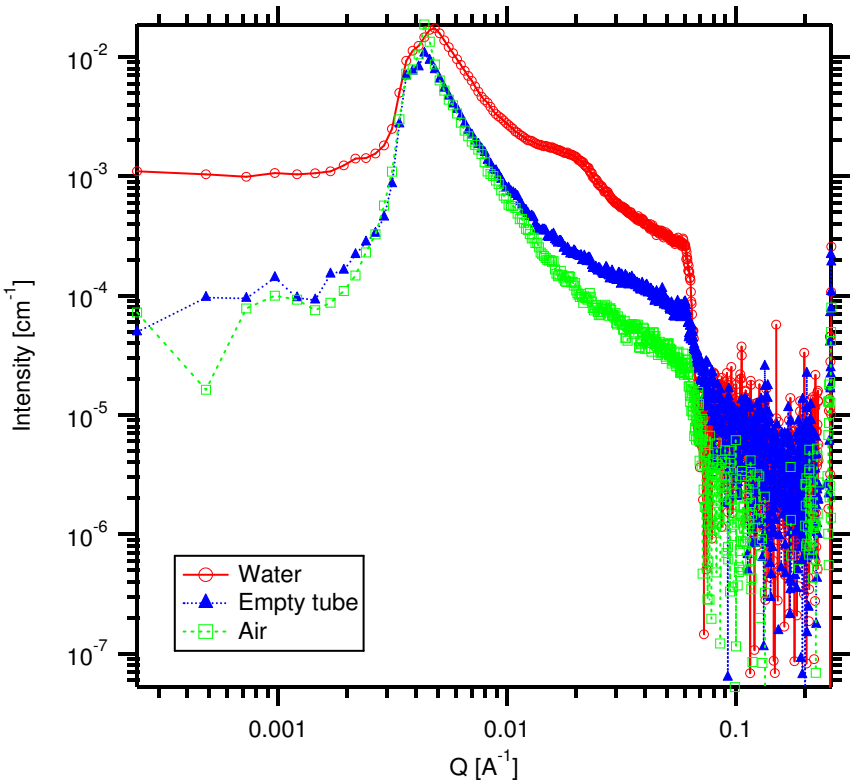

Figure 4.2. SAXS measurements for possible backgrounds (exposure time: 0.05 s)

In Fig. 4.2, the SAXS emissions of air, an empty tube, and water are presented for the same exposure time at room temperature. Clearly, liquids like water scatter significantly relative to the tubes or air. Solvent-background subtraction was performed for all intensity profiles. For each experimental condition, a tube filled with a relevant solvent was in place and emissions were measured concurrently. Fig. 4.3 illustrates the effect of this background subtraction on scattering measurements. Typically the background signal is more than an order of magnitude smaller than the emission of interest. This procedure is the most convenient way to eliminate parasitic scattering, i.e. residual scattering by pinholes, air, sample tube, and scattering due to solvents.

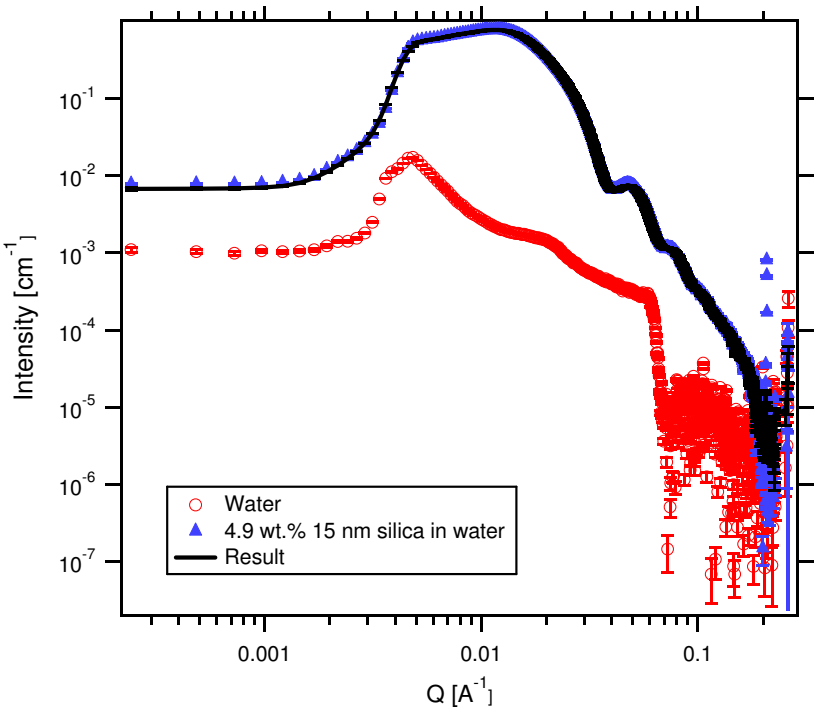

Figure 4.3. Background subtraction for 4.9 wt.% 15nm silica particles in water (exposure time: 0.05 s)

4.3.2.2. Instrumental collimation data correction

In order to obtain sufficient scattered intensity in a small-angle X-ray scattering measurement the experimental stations are usually equipped with a slit collimation system. In this case, the observed intensity does not correspond to that obtained with the pinhole collimator, but to the pinhole intensity averaged (smeared) over

the angular range which is mainly defined by the slit geometry. In this work, the desmearing method developed by James A. Lake was used [52].

If the angular range of X-rays passed by slits when the detector fixed aperture is also small, the relationship between the slit-smeared experimental curve, $I_{0S}(q)$, and the pinhole curve, $I_0(q)$ is given by the following expression.

$$I_{0S}(q) = \int_{-\infty}^{+\infty}\int_{-\infty}^{+\infty}\int_{-\infty}^{+\infty} W_\lambda(\lambda)W_z(z)W_y(y)I_0\left[((q-y)^2+z^2)^{1/2}\right]d\lambda dy dz \qquad (4.1)$$

W_λ, W_z and W_y are the wavelength, slit-height and slit-width weighting functions respectively, the forms of which depend on the collimating system, and which are normalized as seen on (4.2).

$$\int_{-\infty}^{+\infty} W_\lambda(\lambda)d\lambda = \int_{-\infty}^{+\infty} W_z(z)dz = \int_{-\infty}^{+\infty} W_y(y)dy = 1 \qquad (4.2)$$

Equation (4.1) is tractable to iterative approximation methods. Assuming, as an approximation to I_0, an initial trial curve, I_{0T}, it is possible to smear I_{0T} and contrast this smeared trial curve, I_{0TS}, with I_{0S}. Relationships between I_{0TS}, I_{0S}, and I_{0T} may be examined in order to generate a better approximation to I_0. Let us consider I_{NT} as the (N+1)th approximation to I_0; and I_{NTS} as the smear of I_{NT}. If I_0 is larger than I_{NT} at some point and if I_0 and I_{NT} do not decrease more rapidly than the weighting functions W_z and W_y, then the effect of (4.1) is to average I_0 over some region of q. it seems I_{0S} must be larger than I_{NTS} [52]. Equation (4.3) is therefore very reasonable.

$$I_0 - I_{NT} \cong I_{0S} - I_{NTS} \qquad (4.3)$$

For faster convergence, let us multiply the right-hand side of (4.3) by $A=I_{NT}/I_{NTS}$, a positive function of q that improves corrections on $I_{(N+1)T}$ where needed. Equation (4.5) is obtained as the final correcting relationship of this method.

$$I_0 - I_{NT} \cong A \cdot (I_{0S} - I_{NTS}) \qquad (4.4)$$

$$I_0 \cong I_{(N+1)T} = (I_{NT}/I_{NTS}) \cdot I_{0S} \qquad (4.5)$$

As for the selection of the first appropriate trial function, a good choice for this method is the experimental curve, I_{0S}.

Double-crystal collimation greatly simplifies equation (4.1) as the double-crystal collimator used in this work has a wavelength resolution of $\Delta\lambda/\lambda \approx 0.0003$. Therefore, wavelength smearing can be assumed as negligible. Slit-width smearing can also be neglected because of the narrow curve of the CCD analyzer. The only weighting function remaining is then W_z, the slit-height smearing. In the slit-height direction, the detector subtends an angle $\Delta\theta_l$ with a point within the illuminated area of the sample. This angle can be estimated as the ratio of the diameter of the photodiode detector divided by the sample-to-detector distance [53]. The characteristic slit-height in reciprocal space can be calculated by:

$$l_0 = \frac{1}{2}\left[\frac{4\pi}{\lambda}\sin\left(\frac{\Delta\theta_l}{2}\right)\right] \tag{4.6}$$

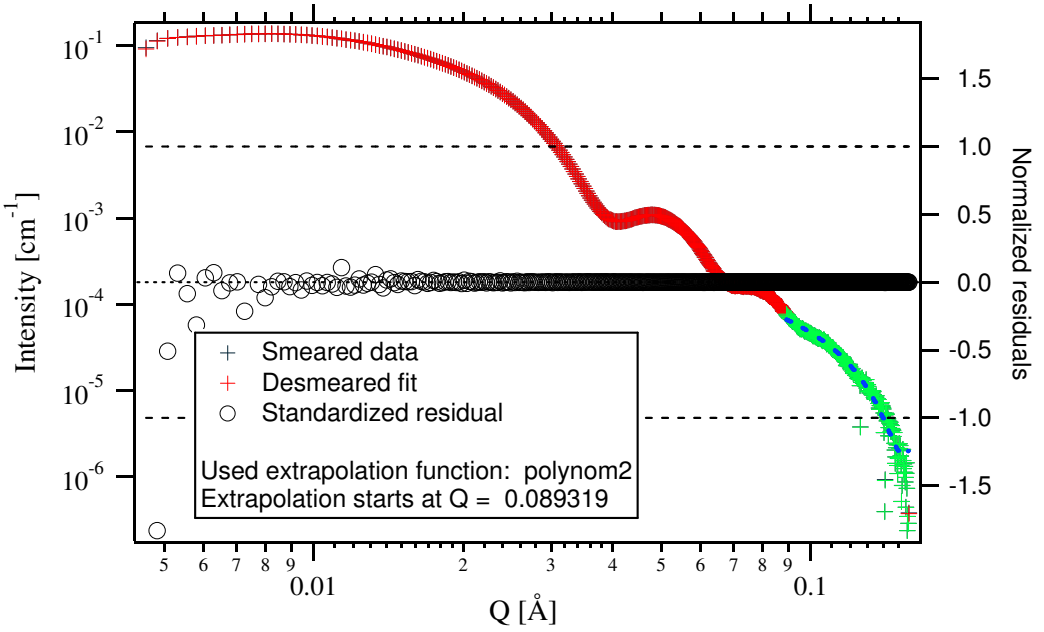

Figure 4.4. Desmearing procedure for 1 wt.% 15nm silica nanospheres in water at 210°C (exposure time: 2 s)

The slit-height value, in reciprocal space, obtained for the experimental conditions used in this work was $l_0 \approx 0.001$ Å^{-1}. Fig. 4.4 illustrates an example of the slit-height correcting method applied on one experimental sample. The desmeared intensity corresponds almost exactly to the experimental (smeared) data. Each case examined was similar. This means that the beam optics at the APS experimental station introduced minimal distortion. Intensity profiles were analyzed without desmearing.

4.3.3. Data analysis

4.3.3.1. Unified Guinier-exponential/power-law model

Recent developments in small-angle scattering show that complex systems may contain multiple levels of related structural features. Greg Beaucage developed a unified model that can represent a wide variety of small-angle scattering spectra with multiple structural levels. Each structural level is described by a Guinier and an associated power-law regime. Special attention was paid while developing the fundamental function so that it could model both the Guinier exponential and structurally limited power-law regimes without introducing new parameters other than those used in the local fits [54-56].

The 'knee' or low-q plateau in the log-log intensity profile represents a region of exponential decay in scattered intensity that corresponds to an average structural size according to Guinier's law. The power law region reflects a constant mass scaling with sizes of measurement according to the various mass or surface fractal scattering laws. This power-law regime is limited at each end by structural limits of this scaling behavior. It is important to note that local and global fits agree well because more data points are used and account is made for overlapping features in the scattering pattern [55].

The concept of a correlation function, $\gamma(r)$, was first introduced by Porod which, in a particulate system, represents the probability that a point at a radial distance r from a given point in a particle will also be in the particle phase. $\gamma(r)$ is related to the form factor $F(q)$ by equation (4.7).

$$\overline{F^2(q)} = V_p {\rho_e}^2 \int_0^\infty \int_0^\infty \int_0^\infty \gamma(r) e^{-i\boldsymbol{q}\cdot\boldsymbol{r}}\, d\boldsymbol{r} \qquad (4.7)$$

As explained in section 3.5, Guinier's law is the Fourier transform of the correlation function for a particle randomly averaged about its orientation and its position relative to the scattering reference frame [45]. Random positioning of the scattering reference frame about the particle structure leads to an average structure described by a radially symmetric probability function as expressed on (4.8). Note that this correlation function contains information only about the average properties of the

particle. Details about the local structure, such as a description of the surface, are completely lost in this averaging [55].

$$\gamma(r)_{Guinier} = e^{-3r^2/4{R_g}^2} \tag{4.8}$$

Fourier transformation of (4.8) according to (4.7) leads to the exponential appearing in Guinier's law. As description of the Guinier regime does not account for local structure, (4.9) can be used in the final unified equation without further modification.

$$I(q) = I_e \overline{N_p} n^2 e^{-{R_g}^2 q^2/3} \tag{4.9}$$

The power-law component of the unified model was derived after Porod's law for a particulate system. The Porod correlation function is described as the probability that two points separated by a distance *r* in an arbitrary direction are in the Porod bulk or in the inner half of the Porod surface (Fig. 4.5) [55].

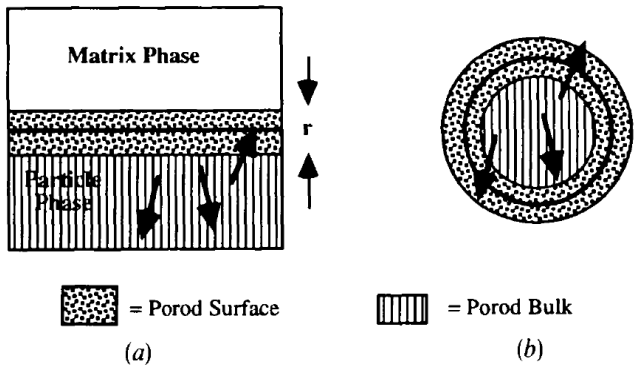

Figure 4.5. Classic Porod scattering (a) and structurally limited Porod scattering (b)
The bold arrows in the figures represent ($\mathbf{r_m - r_l}$) for arbitrary pairs of points in the particle [55].

A probability function that accounts for the probability of translation of the particle along **r,** meeting the Porod condition is expressed in (4.10). This three-dimensional Gaussian function accounts for Brownian diffusion along the three possible axes, considering them as independent of each other [55].

$$p(q, R_g) = \left[\mathrm{erf}\left(qR_g/6^{1/2}\right)\right]^3 \tag{4.10}$$

To account for finite structural effects in power laws, q needs to be reduced to q^*. Beyond an average particle size, q^* becomes rapidly larger as q becomes smaller; this serves to 'cut off' the power law at low-q regime [55].

$$q^* = \frac{q}{\left[\mathrm{erf}\left(qR_g/6^{1/2}\right)\right]^3} \tag{4.11}$$

In the case of centrosymmetric particles that are rotationally averaged, a simplified expression of (4.7) was developed by Debye. Applying the correlation function (4.10) in (4.12), one obtains the form factor for a structurally-limited Porod law [55].

$$\overline{F^2(q)} = V_p {\rho_e}^2 \int_0^\infty p\left(q, R_g\right) \left[\frac{\sin(q^* r)}{q^* r}\right] 4\pi r^2 \, dr \tag{4.12}$$

$$\overline{F^2(q)} = 2\pi {\rho_e}^2 S \left[\frac{\left[\mathrm{erf}\left(qR_g/6^{1/2}\right)\right]^3}{q}\right]^4 \tag{4.13}$$

A description of the structurally-limited Porod law is expressed in (4.14). However, power-law scattering for mass-fractal, surface-fractal or diffuse interfaces is found to be $I(q) \propto q^{-P}$. The value of the scattering coefficient P will determine the type of power-law scattering. For $P = 4$ Porod-law is found. Therefore, (4.14) was implemented on the unified equation (4.15), using the more general expression for power-law scattering, making the model valid for a wider variety of systems.

$$I(q) = 2\pi N_p {\rho_e}^2 S_p I_e \left[\frac{\left[\mathrm{erf}\left(qR_g/6^{1/2}\right)\right]^3}{q}\right]^4 \tag{4.14}$$

$$I(q) = G e^{-{R_g}^2 q^2/3} + B \left[\frac{\left[\mathrm{erf}\left(qR_g/6^{1/2}\right)\right]^3}{q}\right]^P \tag{4.15}$$

where $G=I_e N_p n^2$ is the exponential prefactor, and B is a constant prefactor specific to the type of power-law scattering. Note that both of these prefactors are calculated in the software implementation of the model. For the samples analyzed in this work, only one structural level in the unified model seemed necessary for fitting the scattering curves.

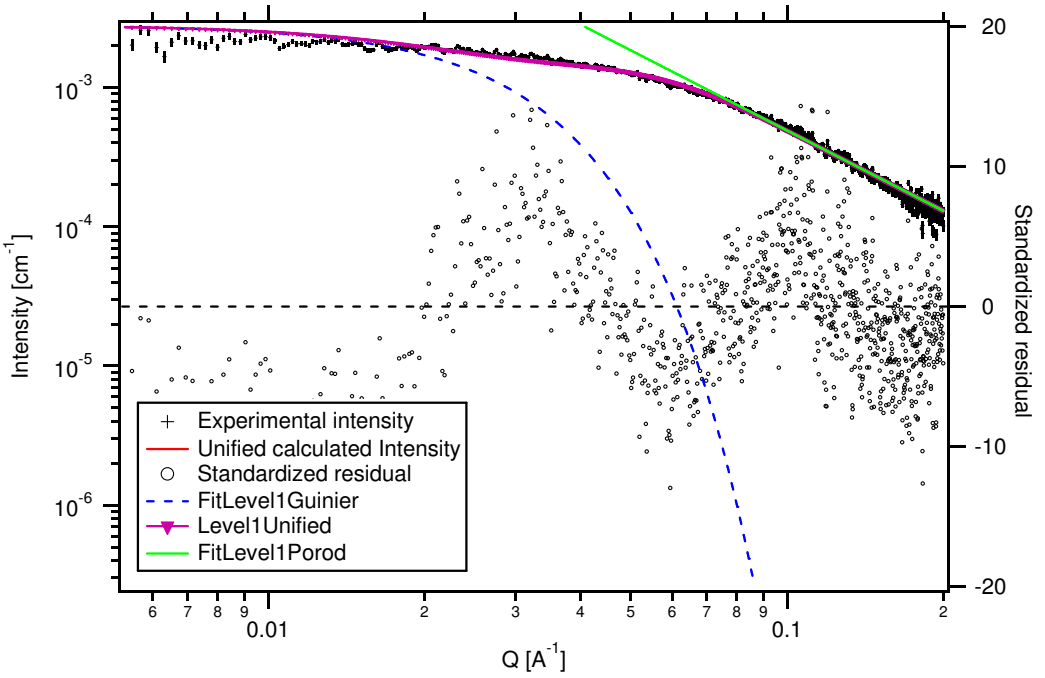

Figure 4.6. Unified model applied to 20 wt.% AB filtrate in n-dodecane at 130 °C (exposure time: 0.02 s)

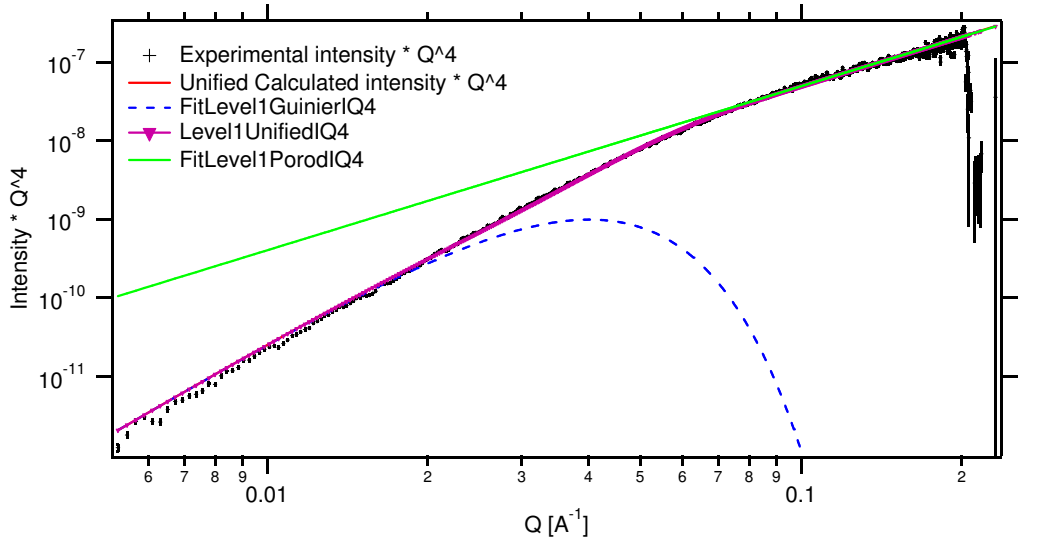

Figure 4.7. Unified model applied to 20 wt.% AB filtrate in n-dodecane at 130 °C - plot $I(q)xQ^4$ vs Q (exposure time: 0.02 s)

In Fig. 4.6, the unified Guinier/power-law model was applied to an example emission experiment. The fit obtained is precise with only small differences arising in the low-q region. For this sample, a radius of gyration of R_g = 55.5 Å, and a scattering coefficient of P = 2.13 were found.

4.3.3.2. Particle size distribution estimation

The general small-angle scattering equation (3.12) was coded using the expression (4.16). Here, a summation over a discrete size histogram substitutes the usual integration over a continuous size distribution. This equation allows the calculation of scattering intensity from particles in multiple populations of scatterers.

$$I(q) = \sum_k |\Delta\rho_k|^2 \, S_k(q) \sum_{i_k} \left|F_k\left(q, D_{i_k}\right)\right|^2 V_k\left(D_{i_k}\right) f_k\left(D_{i_k}\right) \Delta D_{i_k} \qquad (4.16)$$

where the subscript i represents the bins in the size distribution and ΔD_i is the width of bin i. Subscript k denotes different scatterer populations; each population has its own binning index i_k. D is the dimension of the particle (radius for spheres). Volume fraction distribution for scatterers, $f(D)$, was chosen in this model due to greater numerical stability [51]. Volume fraction distribution is related to the more frequently used number distribution $N(D)$ by the following:

$$f(D) = V(D)N(D) = V(D)N_T\psi(D) \qquad (4.17)$$

where $V(D)$ is the volume of the particle, N_T is the total number of scatterers, and $\psi(D)$ is the probability of occurrence of a scatterer of dimension D.

Four different size distributions are available in the *Irena* tool for particle size distribution: Gauss (normal), log-normal, Lifshitz-Slyozov-Wagner (LSW), and power-law. In this work, better fits were encountered for Gauss (normal), and log-normal size distributions.

The size range for particle size distributions was fixed as 10 – 1000 Å, due to experimental limitations of the scattering technique used. With this range in mind, natural binning for the size distributions was performed. This method results in a non-linear step size and uses two input parameters: number of bins, N_b, and fractional volume of scatterers neglected for feasible numerical solving, $2V_N$ (Fig. 4.8), which were chosen as 100 bins and 0.01, respectively.

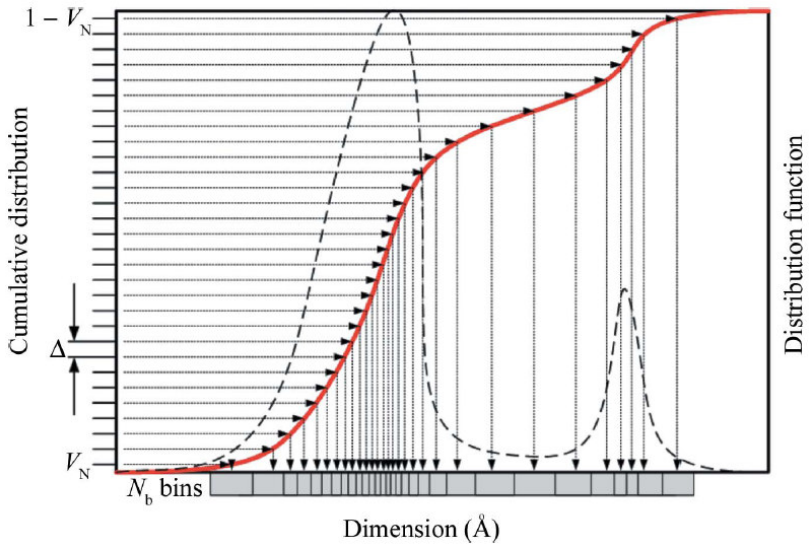

Figure 4.8. Natural binning selection for an arbitrary size distribution [51]

As shown in Fig. 4.8, a cumulative distribution is created by numerical integration of the selected size distribution. The center of the first bin (smallest dimension) is found as the value for which the cumulative function is equal to V_N, and the center of the last bin (largest dimension) is the value for which the cumulative function equals 1 – V_N. The remaining bins are established by selecting associated dimensions at regular increments, Δ, of the cumulative distribution.

$$\Delta = \frac{1-2V_N}{N_b-1} \tag{4.18}$$

The form factor primarily used for the calculations presented in this work was that of a spheroid. As previously discussed in section 3.4, the shape factor for a spheroid is expressed by the following expression:

$$\overline{F^2(q)} = \left(3\frac{\sin(qr)-qr\cos(qr)}{(qr)^3}\right)^2 \tag{4.19}$$

In terms of the structure factor, this tool performs, by default, the modeling as if the samples were in the dilute limit, $S(q) = 1$. However, an approximated model for hard spheres can be implemented in the calculations in order to account for interparticle interference. Parameters included in this interference estimate are k, the packing factor and ζ, the correlation distance.

$$S(q) = \frac{1}{1+3\kappa[\sin(q\zeta)-q\zeta\cos(q\zeta)]/(q\zeta)^3} \tag{4.20}$$

Figs. 4.9 and 4.10 show the estimation of the particle size distribution for a silica nanosphere + water dispersion. In Fig. 4.9 one can judge the quality of the model fit. Further changes in the model parameters or initialization conditions can alter the final fit obtained. For the example in Figure 4.9, a mean radius of 200 Å was obtained with a standard deviation of 21 Å for silica particles with a nominal mean size of 15 nm.

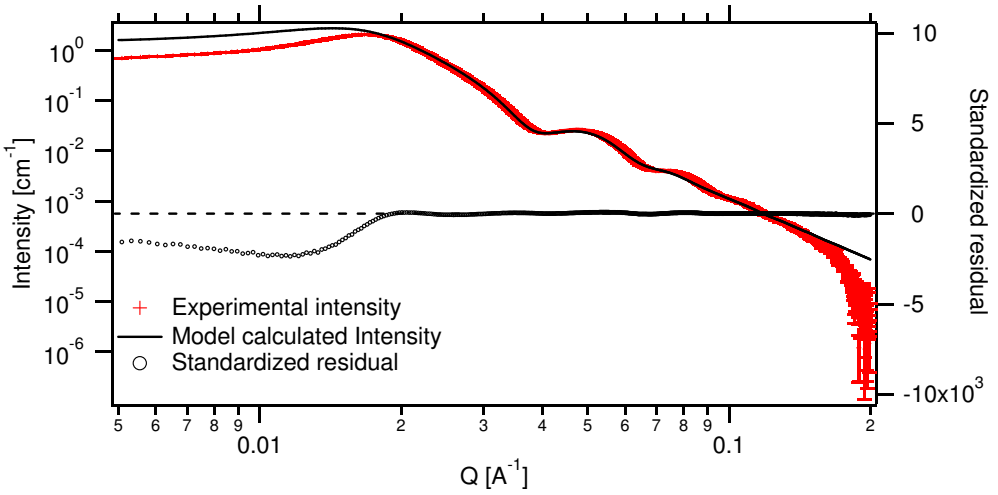

Figure 4.9. Particle size distribution estimation for 16.1 wt.% 15 nm silica nanospheres in water (exposure time: 0.05 s)

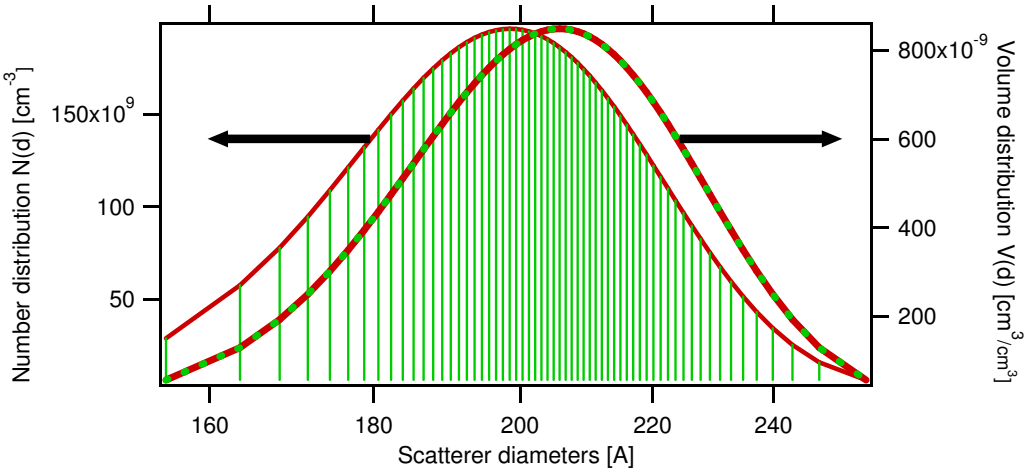

Figure 4.10. Number and volume size distributions for 16.1 wt.% 15 nm silica nanospheres in water (exposure time: 0.05 s)

4.4. Summary

The computational approach selected for this work involves data visualization with the CCD images, as well as numerical methods applied on the intensity profiles for data analysis. The first method chosen was the unified Guinier-exponential/power-law model for which the only input necessary is the number of structural levels. The outputs of this method are the radius of gyration and the scattering power-law. The radius of gyration provides a measure of scatterer size, while the scattering coefficient reflects the fractal or diffuse nature of the scatterers. Particle size distribution is also estimated but for this calculation input parameters include the shape of the scatterers, particle interaction, type of size distribution, and the assumption that particles are dense. Results from both methods provide important structural information about asphaltene behavior and permit discrimination of asphaltene properties based on the method of separation.

Chapter V
METHODS AND MATERIALS

5.1. Introduction

Experimental details are presented in this chapter. It opens with explanations of the methods used, including the asphaltene precipitation and the nanofiltration procedure, and the small-angle X-ray scattering (SAXS) measurements. The materials used are described along with the experimental conditions. It is very important to acknowledge the collaboration and contributions of Ms. Mildred Becerra, Dr. Bei Zhao and Mr. Martin Chodakowski, in this aspect of the work as samples were prepared and nanofiltration and SAXS measurements were performed by them.

5.2. Experimental methods

5.2.1 Asphaltene precipitation

Chemically separated asphaltenes were precipitated following the ASTM D3279 protocol. The separation was induced by addition of n-pentane to Athabasca vacuum residue (AVR) using a solvent to oil volume ratio of 40:1 at room temperature and atmospheric pressure. Mixtures were stirred overnight followed by a two-step vacuum filtration. Mixtures were initially filtered with a Fisher filter paper Q2, with a pore size distribution of 1-5 μm. Permeate were then filtered using a 0.22 μm Millipore membrane containing mixed cellulose esters. The filtration membranes and the flask were washed with n-pentane in order to eliminate residues. This was repeated until the filtrate was clear. The membranes and the precipitated material were then dried at 373 K for 30 min and placed in a vacuum oven overnight [57].

5.2.2 Nanofiltration experiments

Pall Membralox ceramic membranes were used for nanofiltration. The membranes were 250 mm long; with an outer diameter of 10 mm and an inner diameter of 7

mm. Membranes with six different average pore sizes were utilized in a previous research project [22]: 5 nm (γ-alumina), 10 nm (γ-alumina), 20 nm (zirconia), 50 nm (zirconia), 100 nm (zirconia), and 200 nm (γ-alumina). However, only samples obtained from the experiments with the membrane of 20 nm average pore size were examined in the present work. The cumulative pore size distributions of the different ceramic membranes are shown in Fig. 5.1.

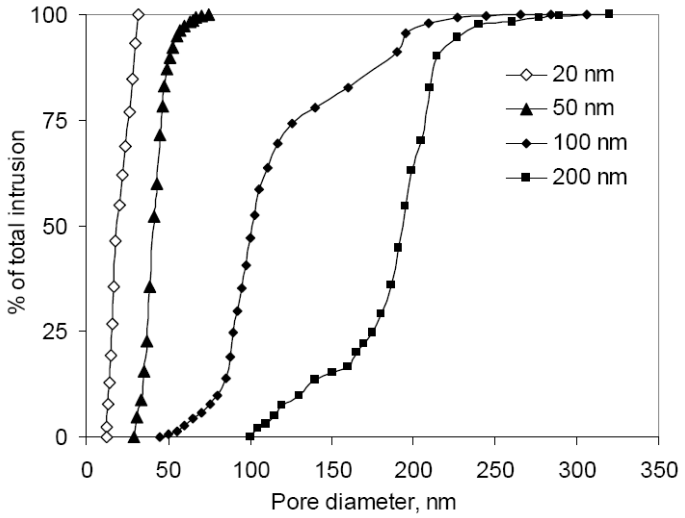

Figure 5.1. Cumulative pore size distributions of ceramic membranes [22]

A diagram of the nanofiltration apparatus is presented in Fig. 5.2. First, the reservoir was purged with nitrogen several times to avoid contamination in the system. The temperature was maintained at 473 K and a pressure drop over the ceramic membrane was always kept below 7 bar using compressed nitrogen. Approximately 200 g of Athabasca bitumen were fed to the reservoir. To minimize the formation of a filter cake in the ceramic membrane, the filtration process was considered as finished once 50 g of permeate was collected. It took about 4 weeks to complete the filtration experiment with the zirconia membrane of nominal size 20 nm [9, 22].

The membranes were only reused for the same feeds. Cleaning the membranes involved soaking them in tetrahydrofuran until the solution was clear. Subsequently, the filter was reassembled and tetrahydrofuran was fed from the shell side to back-flush residues. Finally, nitrogen was used to purge tetrahydrofuran from the filters [9, 22].

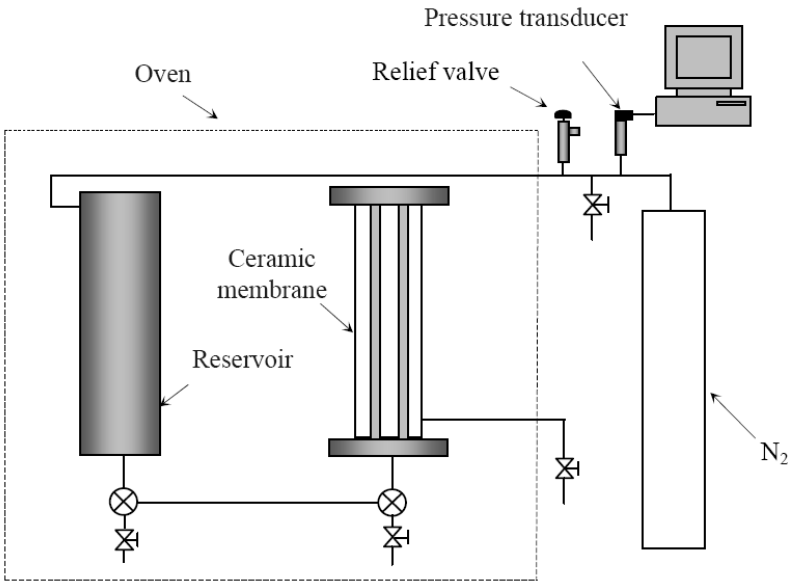

Figure 5.2. Nanofiltration apparatus [22]

Table 5.1. Composition of Athabasca bitumen and filtered samples from 20 nm membrane [22]

	AB feed	**AB permeate**	**AB retentate**
		Elemental analysis, wt. %	
C	83.2	84.3	81.0
H	9.7	10.0	8.6
N	0.4	0.4	0.6
S	5.3	5.0	6.1
O	1.7	1.7	1.9
		SARA analysis, wt. %	
Saturates	16.1	18.4	7.9
	(20)[a]	(21)[a]	(18)[a]
Aromatics	48.5	53.0	21.8
	(60)[a]	(59)[a]	(50)[a]
Resins	16.8	18.2	13.6
	(21)[a]	(20)[a]	(31)[a]
Asphaltenes (C5)	18.6	10.4	56.7
		Metal analysis, mg/kg	
Al	492	4.6	920
Ba	6.4	< 0.1	18.1
K	77	< 1.0	196
Ca	163	67	285
Cr	2.8	1.0	7.7
Fe	762	27	964
Mg	65	8.8	114
Mn	30	4.6	39
Mo	12	1.5	45
Na	91	93	251
Ni	93	64	191
Si	355	92	460
Ti	24	2.2	55
V	247	169	472
Zn	4.4	0.8	7.4

[a] Data are on asphaltene-free base, wt. %

After the nanofiltration experiment samples were collected. Permeate samples were collected from the shell side. Retentate samples were obtained from within the membrane tube. Compositional analyses, reported in Table 5.1, were performed using American Society for Testing and Materials (ASTM) techniques where available. Details concerning chemical and elemental analyses as well as analysis protocols are available elsewhere [22]. For the 20 nm filtered samples, the elemental analysis feed, permeate and retentate are similar, while from the SARA analysis, it is clear that the main effect of filtration is to enrich the asphaltene content on the retentate. However, smaller asphaltene aggregates did pass through the 20 nm membrane, and they constitute 10.4 wt. % of the permeate. The saturates, aromatics, and resins content of all samples remained unchanged [26], within experimental error on an asphaltene-free base [9]. Mineral matter is also enriched in the retentate.

5.2.3 Small-angle X-ray scattering measurements

The small-angle X-ray scattering (SAXS) experiments were performed at the BESSRC-CAT 12ID-C experimental station at the Advanced Photon Source (APS) facility in the Argonne National Laboratory. This third-generation synchrotron radiation source possesses a ring energy of 7 GeV, and provides tunable quasi-monochromatic radiation from undulators with energies of 1-40 keV, and white radiation from wigglers to over 100 keV [58].

The layout of the storage ring and other accelerator components are shown in Fig. 5.3. First, a 200 MeV linear accelerator produces 3 A electron pulses of 16.5 ns width. This beam is converted to 25 mA positron pulses using a tungsten target and later accelerated to 450 MeV. The positrons reach the 7 GeV ring energy in the booster synchrotron of 367 m circumference. Finally, the positrons are injected into the rf bunches in the 1060 m circumference storage ring, where a 100 mA operational current is achieved [58]. This high-energy photon flux can later be used in one of the 66 beamlines currently available at APS.

Normally at APS, each photon beamline comprises four functional sections. The first section is the insertion device (ID) or bending magnet (BM) that provides the radiation source. The second section contains the safety shutters, masks, and other

elements to define the emerging X-ray beam. The third section comprises the hard X-ray optics, crystals and/or mirrors, which will provide the monochromatization required for the experiments. The last section is the experimental station, where investigations are performed [58].

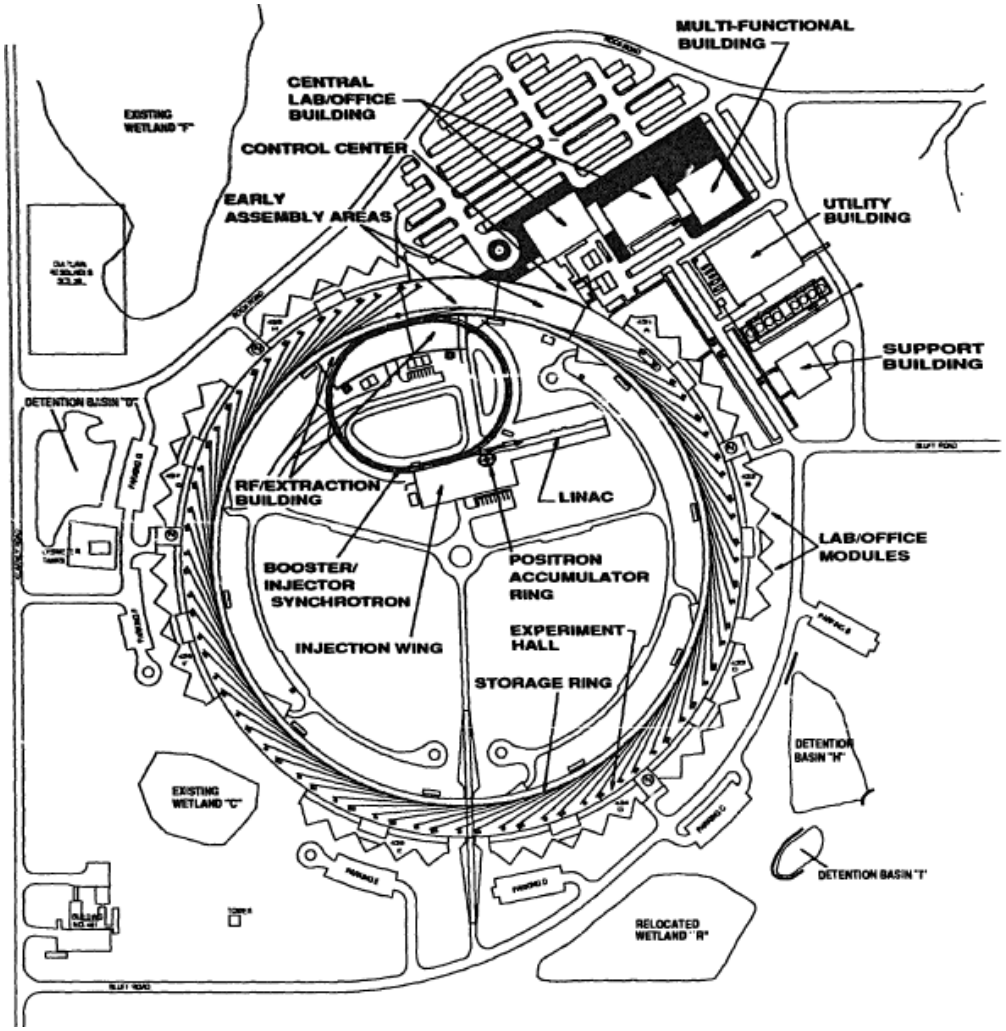

Figure 5.3. Plan view of the Advance Photon Source at Argonne National Laboratory [59]

The beamline employed for this work was the BESSRC-CAT 12ID. The insertion device used in this beamline was the Hybrid Undulator A that covers energies of 3.2-13 keV in the first harmonic and to about 39 keV in the third harmonic. Along with the undulator, a high-vacuum operation double crystal monochromator was used in this beamline (Fig. 5.4). The experimental station 12ID-C is used for small-angle scattering experiments and atomic physics. The station is equipped with a high-resolution (3000 x 3000 pixels) large format mosaic CCD detector [60].

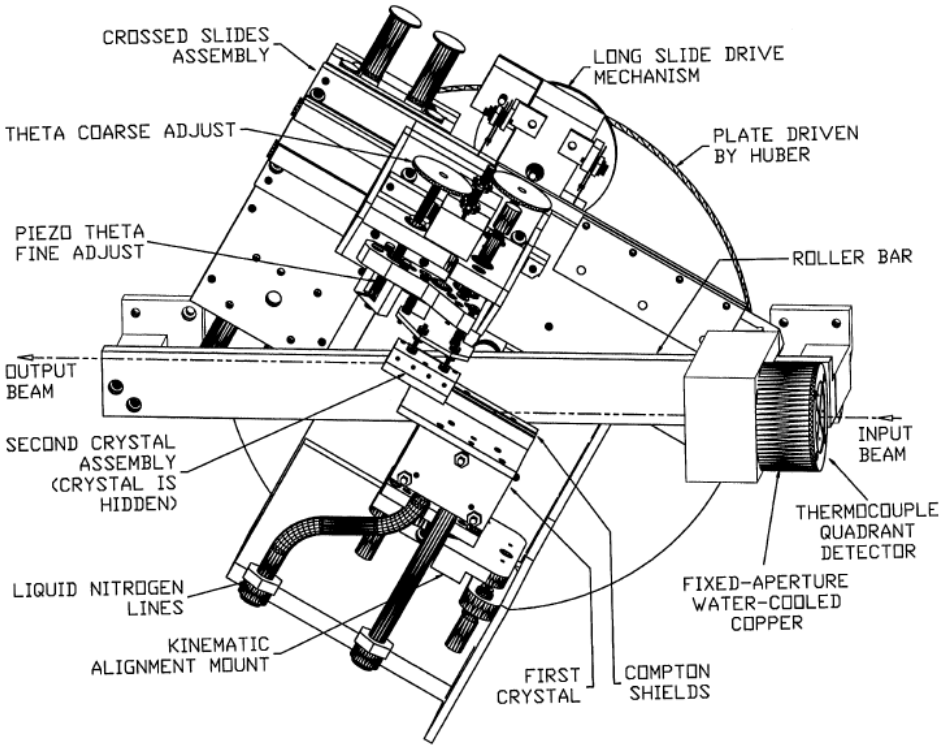

Figure 5.4. Schematic view of the cryogenically cooled BESSRC monochromator [60]

The experiments were performed with photon flux energy of 18 keV, for which the beamline optics had to be adjusted. Also, the CCD images were collected at a sample-to-detector distance of 3.7 m, corresponding to a usable q-range of 0.005-0.2 $Å^{-1}$. Due to the nature of the experiments, a custom multi-sample sample holder was designed by Martin Chodakowski. This sample holder, shown in Fig. 5.5, was constructed from 6061-T6 alloy aluminum, and contains thirteen 3 mm diameter windowed sample wells with matching venting holes. This device was built with six 0.5 in diameter cartridge heater wells to provide uniform temperature along the sample tubes. Two 250 W 120 V cartridge heaters were located in the top of the lid, while four 300 W 120 V cartridge heaters were positioned in the bottom of the main body. The instrumentation used comprised two metal-sheathed 1/16 in diameter type K thermocouples; and a pair of 1/16 DIN size Watlow series 93 PID controllers to independently control the base and lid temperatures. A pair of Watlow DIN-A-MITE A power controllers were also included in the instrumentation of the sample holder.

Synchrotron acquisition times are very fast. However, special care was paid to keep the length of the beam path short, less than ~ 3 mm, in order to avoid multiple scattering [61]. In this work, 3 mm diameter closed-end precision-ground borosilicate glass NMR tubes (Wilmad-LabGlass 335-PP series) were used to prevent this issue. These tubes also allowed confidence in the measurements, since uniformity in the sample tube wall thickness was not a concern. Therefore, further background subtraction was not necessary for the sample tubes.

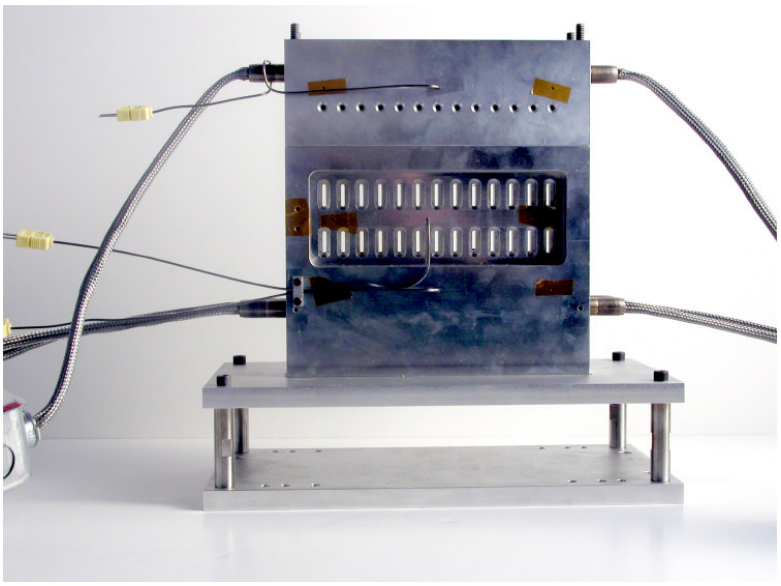

Figure 5.5. Front view of the custom-made heated sample holder

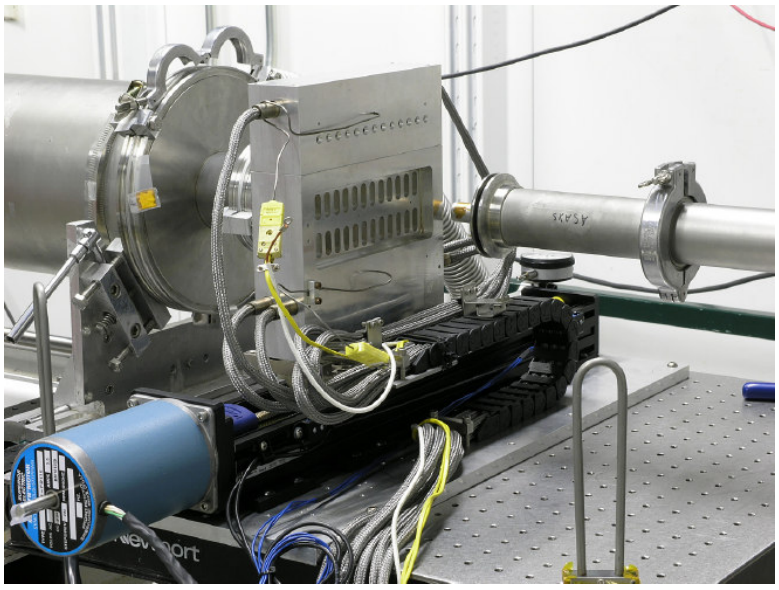

Figure 5.6. Heated sample holder during operation at the APS synchrotron facility

All samples were prepared within the corresponding sample tube. This was done to eliminate any concerns that a non-representative aliquot might be withdrawn from a large mixture prepared *ex-situ*. In addition, magnetically agitated steel balls were employed to mix samples. Finally, the open ends of the tubes were sealed to avoid evaporation during experiments. An example of a prepared sample tube is shown in Fig. 5.7.

Figure 5.7. Sealed sample tube with magnetically agitated steel ball

Once the beamline optics were adjusted and the sample holder was installed, the experimental procedure below was repeated as needed:

1. The temperature set-point of the sample holder was adjusted.
2. Once the sample holder temperature reached the set-point, 15 minutes was allowed to elapse.
3. A pair of magnets was used to mix the contents of the sample tubes.
4. The X-ray beam was passed through the samples, at two elevations, and the SAXS images were collected with 3 repetitions for each exposure time tested.

The experimental conditions tested during the synchrotron measurements are summarized in Table 5. 2.

Table 5.2. SAXS experimental conditions tested

Sample group	Temperature, °C	Exposure time, s
Silica nanospheres in water	25	0.05, 0.1, 0.2, 0.5, 1.0, 2.0, 5.0, 10
AB-permeate in diluents	70, 90, 110, 130, 150, 170, 190, 210, 230, 250, 270, 290, 310	0.01, 0.05, 0.1, 0.5, 1.0
AVR-asphaltenes in diluents	50, 70, 90, 110, 130, 170, 190, 210, 230, 250, 270, 290, 310	0.005, 0.02, 0.5

5.3. Materials

Spherical silica nanoparticles dispersed in water were provided by EKA Chemicals, Inc. Table 5.3 reports the original concentrations of the silica particle + water suspensions. The particle sizes reported are the nominal mean radius of the silica nanospheres. These samples were diluted in distilled water to achieve desired experimental concentrations.

Table 5.3. Concentration of silica nanoparticle dispersions provided

Particle nominal size, nm	Concentration, wt. %
5	16.16
10	21.33
15	39.78
20	40
35	50.49
40.7	51

Athabasca bitumen was originally obtained from Syncrude Canada, Ltd. This sample was characterized as a coker feed obtained from mined bitumen subjected to upstream warm-water extraction, naphtha dilution, and naphtha recovery by distillation between 250 and 350 °C. Thus, volatile constituents initially present may have been lost during sample preparation. Athabasca vacuum residue (AVR), was also obtained from Syncrude Canada, Ltd. This sample consists of the bottoms product from vacuum distillation at 3-5 kPa of Athabasca bitumen. The properties and product specifications for Athabasca bitumen and Athabasca bitumen vacuum bottoms are listed in Table 5.4.

Table 5.4. Properties for Athabasca bitumen and Athabasca vacuum residue [62]

	Bitumen	Vacuum residue
° API Gravity	7.0	1.6
Density, kg/m^3	1021.7	1063.1
Sulfur, wt. %	4.8	5.7
Nitrogen, wppm	4296	5820
MCR (solids free), wt. %	13.6	20.7
Solids (toluene insolubles), wt. %	0.24	0.36
Nickel, wppm	82	125
Vanadium, wppm	210	319

Athabasca bitumen (AB) permeate and Athabasca vacuum residue (AVR) asphaltenes were obtained as explained in sections 5.2.2 and 5.2.1, respectively. More details on the samples examined in this work are presented in Tables 5.5 and 5.6.

Table 5.5. Samples analyzed in this work

Material	Diluent	Concentration, wt. %
Silica nanospheres 5, 10, 15, 20, 35, 40 nm	Distilled water	1.0, 2.0, 5.0, 10.0, 16.0, (30.0)*
AB-permeate	1-methylnaphthalene	10, 20, 40, 80 (1.0, 2.1, 4.2, 8.3)**
AB-permeate	n-dodecane	10, 20, 40, 80 (1.0, 2.1, 4.2, 8.3)**
AB-retentate	1-methylnaphthalene	10 (5.6)**
AVR-asphaltenes	1-methylnaphthalene	0.96, 2.1, 4.0, 7.5
AVR-asphaltenes	n-dodecane	1.0, 2.0, 4.3, 8.2, 16.2

* not possible for 5 and 10 nm silica nanoparticles
** Asphaltene wt.%

Table 5.6. Product information of diluents used

Diluent	Grade	Purity, %	Supplier
1-methylnaphthalene	Reagent	97.0 +	Acros
n-dodecane	HPLC	99.0 +	Aldrich

Chapter VI
RESULTS AND DISCUSSION

6.1. Introduction

This chapter presents the Athabasca asphaltene aggregate size, size distribution, and structure results extracted from the SAXS emission data. Special attention is paid to measurement quality and to the nature of the samples examined, as physically and chemically separated asphaltenes may display intrinsic differences. Model-independent and model-dependent structural analyses are discussed separately.

6.2. Measurement Quality

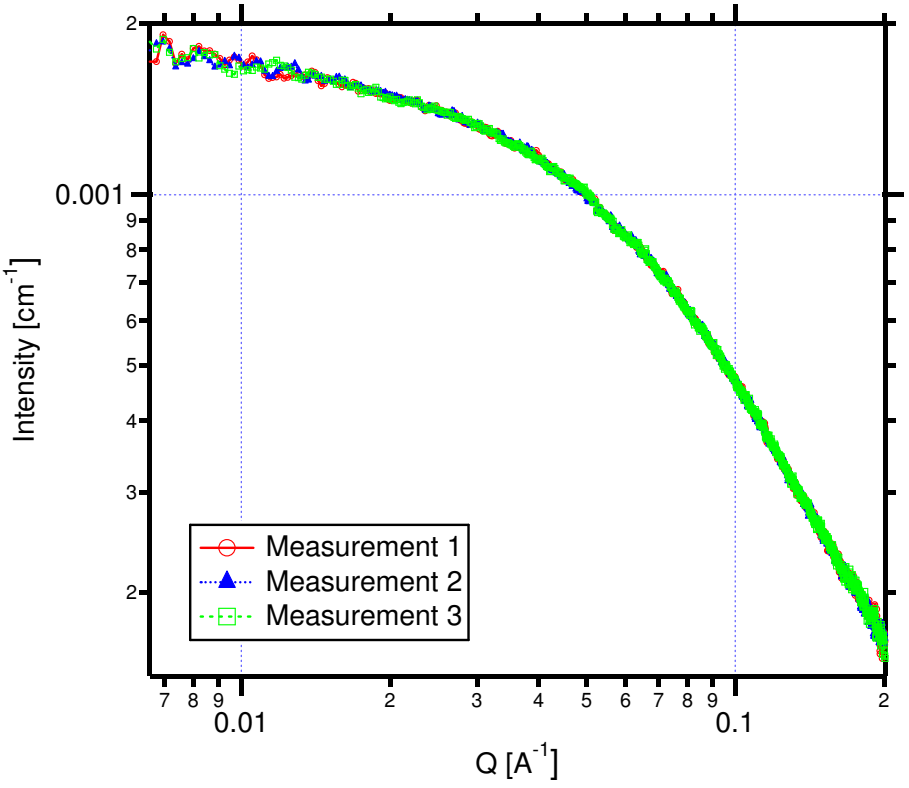

Figure 6.1. Repeatability of SAXS measurements for 20 wt. % AB-permeate in C-12 at 110 ˚C (exposure time: 0.5 s)

At a synchrotron, the speed of individual measurements is short - less than 1 s. This permits multiple exposures, at the same temperature, composition and beam alignment. The repeatability of emissions measurements is illustrated in Figure 6.1 for 20 wt. % AB-permeate in n-dodecane at 110 ˚C. All cases evaluated are similar. The repeatability of model-independent radii of gyration, and scattering coefficient values derived from emissions data using the unified Guinier-exponential/power-law approach is illustrated in Table 6.1 for 20 wt. % AB-permeate in n-dodecane. These results are typical. For all experiments, radii of gyration fall within +/- 5 angstroms, while scattering coefficients fall within 0.1. The means and standard deviations of the model dependent size distributions are equally well defined. Several examples are shown in Table 6.2.

Table 6.1. Repeatability of unified model for 20 wt. % AB-permeate in n-dodecane

Temp.	Radius of gyration (Å)			Std. dev.	Scattering coefficient			Std. dev.
(˚C)	1	2	3	(Å)	1	2	3	
70	62.4	63.4	62.1	0.7	1.96	1.94	1.98	0.03
90	60.5	61.2	60.6	0.4	1.96	1.94	1.96	0.01
110	58.9	56.4	57.8	1.3	1.95	2.04	1.97	0.04
130	60.6	60.9	60.9	0.2	1.90	1.91	1.91	0.003
150	60.3	58.3	59.5	1.0	1.90	1.95	1.91	0.03
170	57.7	59.1	59.4	0.9	1.97	1.90	1.94	0.04
190	59.0	59.3	59.1	0.1	1.94	1.94	1.94	0.001
210	60.2	59.9	59.2	0.5	1.91	1.93	1.93	0.01
230	57.0	59.3	58.3	1.2	2.02	1.94	1.99	0.04
250	57.9	58.1	57.9	0.1	2.03	1.99	2.03	0.02
270	59.8	59.4	57.5	1.2	2.04	2.06	2.08	0.02
290	60.8	61.8	63.1	1.1	2.08	2.03	1.98	0.05
310	62.2	61.3	60.8	0.7	2.16	2.15	2.15	0.01

Table 6.2. Repeatability of particle size distributions for 80 wt. % AB-permeate in n-dodecane

Temp.	Distribution mean (Å)			Std. dev.	Half height full width (Å)			Std. dev.
(˚C)	1	2	3	(Å)	1	2	3	(Å)
70	40.3	40.2	39	0.7	8.7	9	8.8	0.2
90	39.1	40.3	39.9	0.6	9	8.6	9	0.2
110	33.3	37.6	38.6	2.8	9.6	8.6	8.7	0.6
130	41.6	40.8	41.4	0.4	9.5	11	11.5	1.0
150	40.9	41.1	40.9	0.1	9.2	9.4	8.8	0.3
170	40.2	40.3	41.6	0.8	9.3	8.3	12.5	2.2
190	41.1	41.9	41.9	0.5	9.8	11.1	11	0.7
210	39.8	40.7	41.3	0.8	8.1	10.4	10.5	1.4
230	41.7	41.6	41.2	0.3	8.2	8.5	8.2	0.2
250	39.2	40.3	41.4	1.1	11.5	12.1	13.5	1.0
270	40.3	41.6	41.2	0.7	8.5	10.9	9.8	1.2
290	38.8	38.4	39.9	0.8	11.3	10.1	11.4	0.7
310	42.9	41.4	41.6	0.8	9.3	9.3	9.1	0.1

6.3. Model-independent structural analysis of Athabasca asphaltenes

As explained in section 3.5, few size and structure parameters can be extracted from a SAXS emission profile if the nature of the scatterers is not known *a priori*. As little information is known about asphaltenes, the need for model-independent studies is apparent. Given the repeatability of the emissions measurements, even a cursory examination of the emissions data reveals significant differences among the samples as illustrated in Fig. 6.2 for chemically separated asphaltenes and diluted permeate with 4 wt % asphaltenes at 70 °C, in n-dodecane and 1-methylnaphthalene. As the permeate comprises 10.4 wt % asphaltenes, the sample composition is 4 wt. % asphaltenes, 36 wt. % maltenes and 60 wt. % diluent.

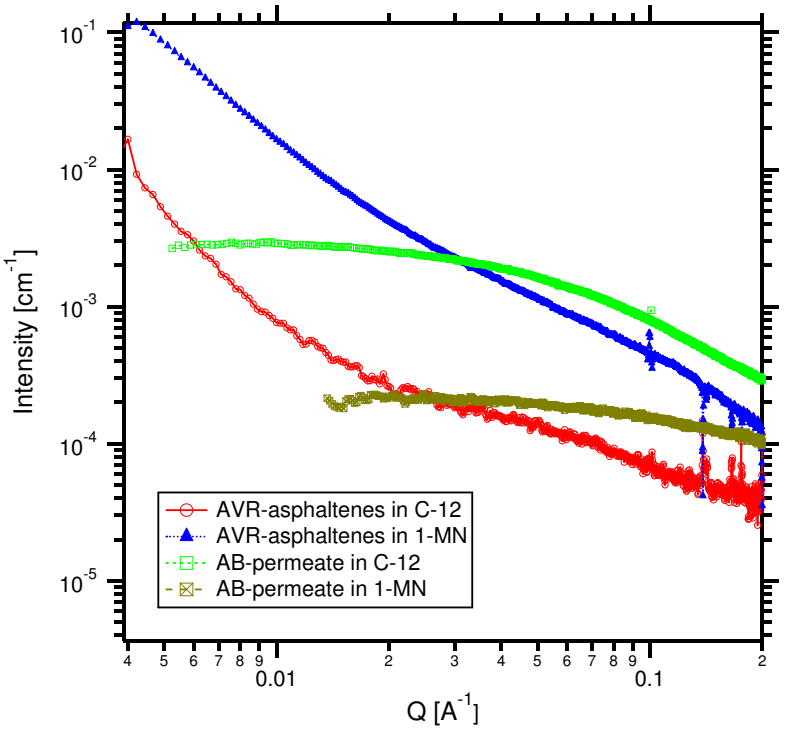

Figure 6.2. SAXS intensity profiles for 4 wt. % asphaltenes in diluents at 70˚C and exposure time 0.5s

The Athabasca bitumen permeates display a low-*q* plateau followed by power-law scattering. This is the ideal scenario for small-angle scattering analysis since this low-*q* feature allows the extraction of size information, and the power-law scattering provides insights into internal structure. The chemically separated asphaltenes, exhibit only power-law scattering in the low- to mid-*q* range. Thus only

information about internal structure can be extracted from the data in a model independent manner. This latter scattering pattern can be attributed to significant differences in the electron density between the electron-rich and highly aromatic, asphaltene aggregates and the diluents; large aggregate sizes that are not observable in the experimental window of the technique; or inter-aggregate particle interactions that result in a structure factor greater than unity [63].

Diluents also play an important role in the behavior of asphaltene aggregates. Asphaltenes are generally defined as the heavy end component of petroleum material that meets a solubility class, soluble in toluene but insoluble in aliphatic diluents [12]. From this reading of the literature, n-dodecane should facilitate aggregation whereas 1-methylnaphthalene should inhibit aggregation and depending on the interactions with the aggregates, even act as a dispersant. For Athabasca bitumen permeates, this seems to be the case: stronger scattering with a higher low-q plateau is observed with n-dodecane as diluent, while a flatter emission profile is obtained in 1-methylnaphthalene. On the other hand, Athabasca vacuum residue asphaltenes show the opposite behavior in the experimental window of these experiments. Stronger scattering is observed with 1-methylnaphthalene. However, since the experiments were only able to provide us with the power-law tail of the SAXS emission profiles, very little can be inferred about the diluent effect on aggregate size for chemically separated asphaltenes. As it was previously explained, this excess scattering is not only an indication of larger scatterer size, but it could also be larger electron density contrast between the asphaltene aggregate and the diluent, or interactions (either attractive or repulsive) between the diluent and the aggregates that result in larger structure factors. In order to obtain an actual value of the structure factor, the scattering intensity needs to be decoupled into separate form and structure factors. However, this task is not feasible for polydispersed scatterers [43]. Also, to understand the role of the diluent electron density, contrast variation must to be used. The characteristics of small-angle scattering of neutrons, makes it easier to perform such a procedure in comparison with SAXS. In small-angle X-ray scattering, the diluent electron density can be changed by addition of various contrasting agents such as sucrose, glycerol or salts and the labeling can be done by isomorphous replacement using heavy-atom labels [41]. As the complexity of this technique is evident and further planning

needed to be done prior to the synchrotron measurements, it was not tested. Usually, the origin of the low-*q* behavior for chemically-separated AVR asphaltenes is inferred from the literature or other types of observations.

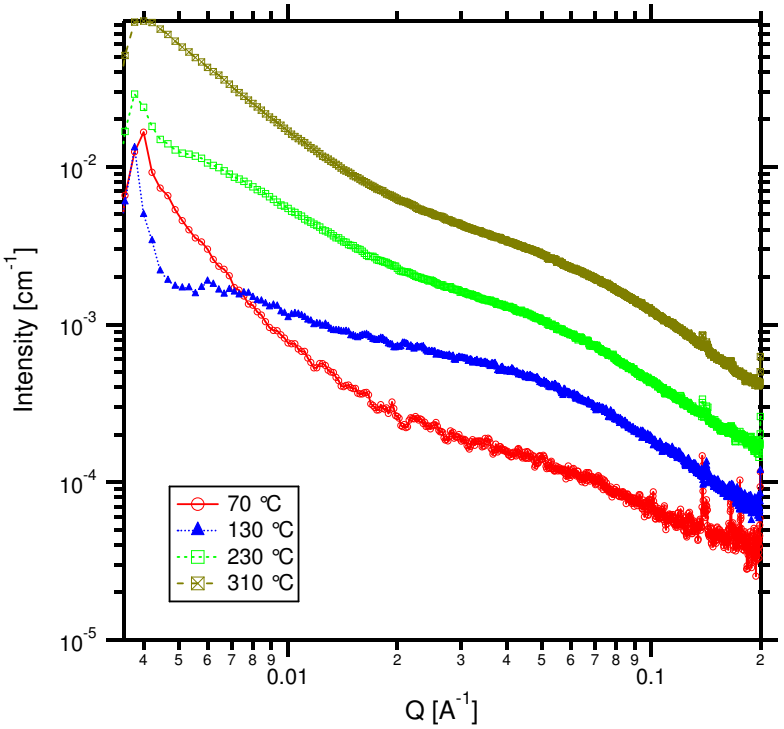

Figure 6.3. 4.3 wt. % AVR-asphaltenes in n-dodecane and exposure time 0.5s

Asphaltenes, on their own, undergo a complex phase transition from ~20 ˚C to more than ~250 ˚C [57, 64]. Fig. 6.3 shows the impact of temperature on the SAXS emissions for 4.3 wt. % Athabasca vacuum residue asphaltenes in n-dodecane. The slope of the power-law tail changes with temperature. Details on this subject are discussed in section 6.2.2.

Fig. 6.4 shows the impact of temperature on the SAXS emission profiles of 4 wt. % AVR-asphaltenes in 1-methylnaphthalene. In this case, little difference is observed in the emissions, suggesting that asphaltene aggregate size, scattering contrast, or structure factor are temperature invariant. Stoyanov et al. [65] conducted molecular simulations on asphaltene disaggregation. The simulations were based on the application of the 3D-RISM theory along with the density functional theory (DFT) Harris approximation, and Hirshfeld and Mulliken population analyses methods for atomic charge calculations. Stoyanov and collaborators found that the potential

mean force (PMF) variation, i.e PMF_{473K} – PMF_{298K}, of Maya asphaltenes in 1-methylnaphthalene was of + 0.4 kcal/mol. This served as an indication that asphaltene disaggregation was not favoured by heating in 1-methylnaphthalene. The PMF variation for Maya asphaltenes in quinoline was – 2.4 kcal/mol, meaning that there was a lower PMF barrier for disaggregation at 473 K than at room temperature. The same solvent effect was also observed in a different study of structural relaxation on Khafji, Maya, and Iranian-Light asphaltenes in the temperature range 373-673 K, using molecular dynamics simulations based on potential energy calculations [66].

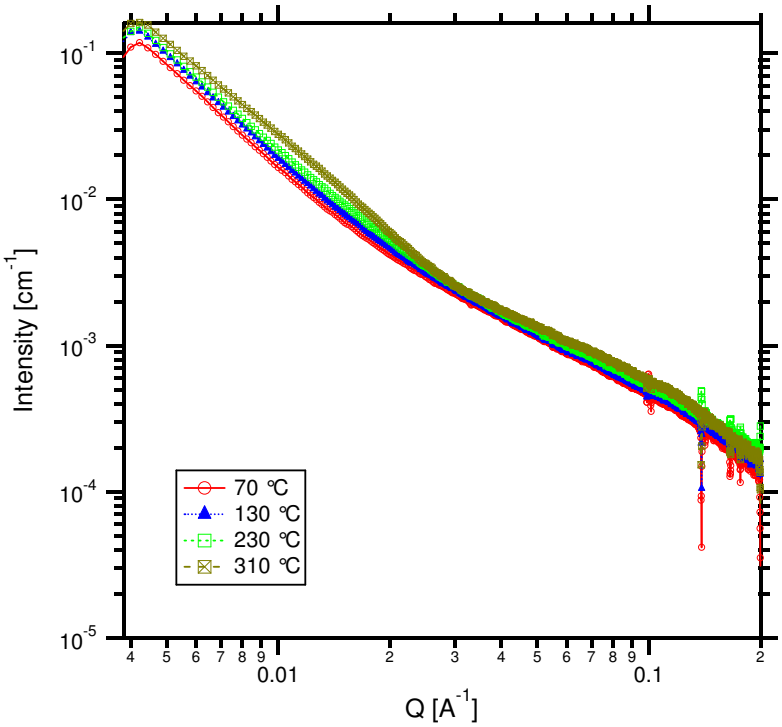

Figure 6.4. 4 wt. % AVR-asphaltenes in 1-methylnaphthalene and exposure time 0.5s

6.3.1. Radius of gyration

The radius of gyration was obtained using the unified Guinier-exponential/power-law model based on Beaucage functions [55], as described in section 4.3.3.1. This analysis allows for joint extraction of radius of gyration and scattering coefficient values from SAXS intensity profiles. Headen et al. [34] have shown the advantage of extending the measurements towards lower-*q* values with ultra or very small-angle scattering in order to attain the Guinier plateau for precipitated-asphaltene samples.

Radii of gyration of up to 470 nm were found in that study. For SAXS measurements, the observable range is limited to less than 100 nm.

For permeate samples, the radii of gyration values for asphaltenes fell well within the size range appropriate for SAXS measurements. This is in part due to the nanofiltration procedure. Permeates passed through a 20 nm membrane. Also, as occurs in any filtration experiment there is always a reduction in the effective pore size of the membrane as the retentate starts to build up on the membrane surface. Thus the initial size of aggregates is less than 20 nm. The impact of temperature and dilution on size and structure are among the variables of interest.

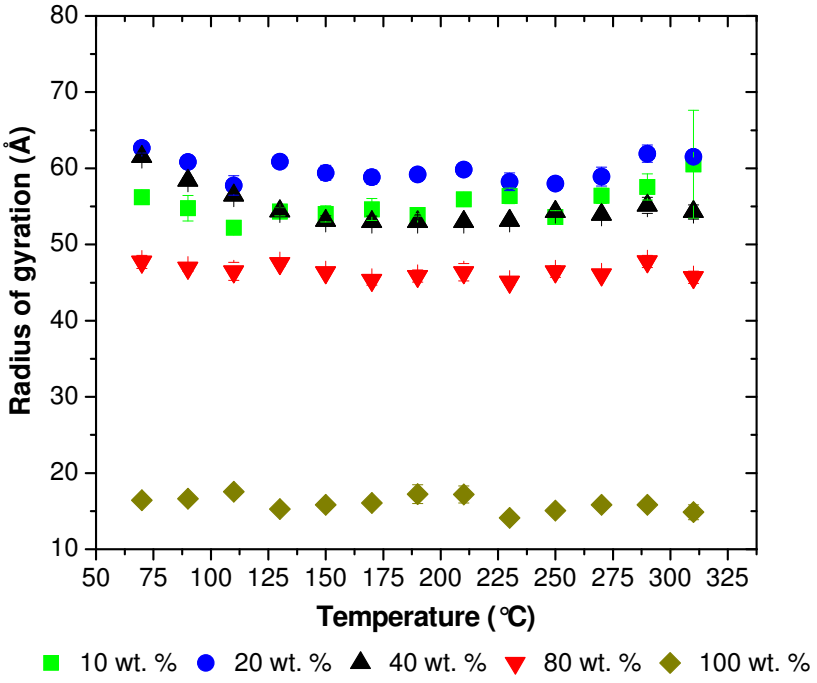

Figure 6.5. Average radii of gyration for scatterers in AB-permeate (wt. %) in n-dodecane

Results for AB-permeates in n-dodecane are presented in Fig. 6.5. Radii of gyration values are weakly dependent on asphaltene wt % but are temperature invariant within experimental error. Radii of gyration are in the range of 15-65 Å and decrease at higher permeate concentrations. These results agree with prior investigations for highly diluted chemically separated asphaltenes in diluents. For example, Sheu [11] showed for SAXS and SANS measurements on Ratawi asphaltenes, radii of gyration at room temperature were in the range of 25-45 Å.

Sheu observed that asphaltene concentration did not affect the radius of gyration significantly, and concluded that these scatterers corresponded to elementary asphaltene aggregates. Similar size ranges for radius of gyration have also been reported elsewhere [6, 27, 31, 35].

In 1-methylnaphthalene, temperature has no impact on radius of gyration and the values are significantly smaller than the values in n-dodecane. 1-methylnaphthalene acts as an aggregation inhibitor but it is not a disaggregating agent. Savvidis et al. [3] also found that asphaltenes recovered by filtration comprise strongly aggregated structures; and that even in toluene they did not disaggregate. They further suggested that aggregation of filtered asphaltenes occurs as a slow clustering of elementary aggregates. Following their reasoning, one might expect aggregates in the permeates to be to stable toward aggregation and disaggregation.

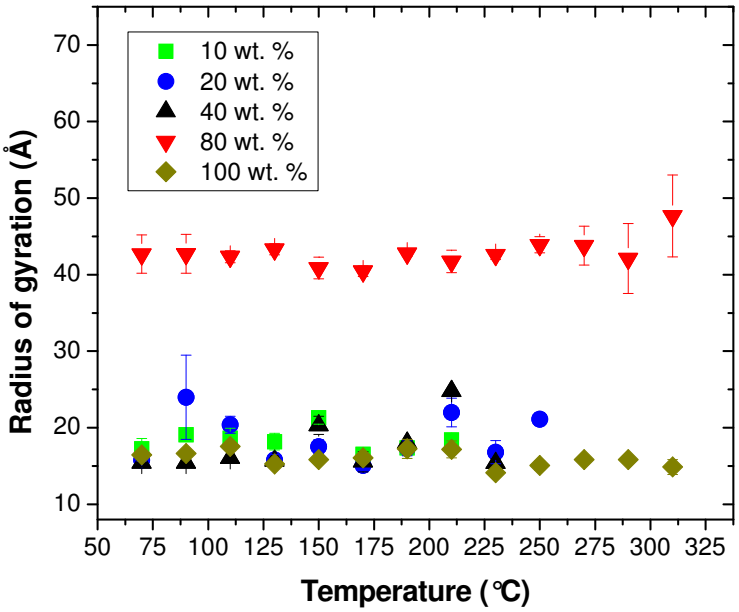

Figure 6.6. Average radii of gyration for AB-permeate (wt. %) in 1-methylnaphthalene

Results for radii of gyration of scatterers in AB-permeate + diluent mixtures are summarized on a temperature independent basis in Fig. 6.7. It is evident that even though the radii of gyration remain in the size range proposed for elementary asphaltene aggregates, the nature and concentration of diluents has a clear effect on aggregate size. The 80 wt. % AB-permeate in 1-MN result appears anomalous but does not disrupt the trend of the data. Aggregates are small in the permeate, and

remain small on dilution with 1-methylnaphthalene. So, 1-methylnaphthalene has no impact on aggregate size. On addition of n-dodecane to AB-permeate, the aggregate radii grow from approximately 20 Angstroms to 60 Angstroms.

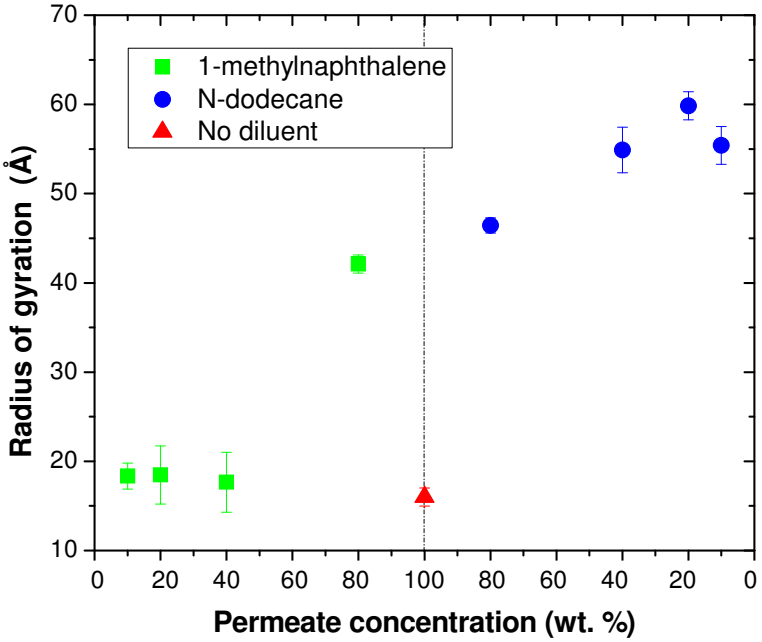

Figure 6.7. Effect of diluent in radii of gyration for AB-permeates

6.3.2. Scattering coefficient

Multiple interpretations have been provided for scattering coefficients in small-angle scattering as noted in chapter III. Values are frequently associated with specific particle shapes [27, 30, 35, 67], and with aggregation models such as DLCA and RLCA [5, 6, 68, 69]. Beaucage [56] listed the scattering coefficients obtained for some structures. Assigning a particle shape or attempting to define a structure based solely on a scattering coefficient value constitutes an over interpretation as values for diverse structures overlap. The goal of this study is not to define asphaltene aggregate shape or structure; but to rather examine the evolution in the scattering coefficient with the experimental conditions. Changes in scattering coefficient embody the evolution in aggregate structure, without a need to specify the shape or structure of asphaltene aggregates.

Table 6.3. Mass-fractal power-law scattering [56]

Mass-fractal structures	Scattering coefficient
Polymers	
Polymer in good solvent	1.5
Self-avoiding walk (linear swollen polymer)	1.67
Random walk (polymer in theta solvent)	2.0
Swollen branched polymer	2.0
Randomly branched ideal polymer	2.29
Non-equilibrium growth processes	
Multiparticle diffusion limited aggregate	1.8
Percolation cluster	2.5
Diffusion limited aggregate	2.5
Low-dimensional objects (apparent mass fractals)	
Randomly distributed rods	1.0
Randomly distributed lamellae or platelets	2.0

6.3.2.1. Scattering coefficients of chemically separated samples

The scattering coefficients for AVR-asphaltenes are shown in Fig. 6.8 (1-4 wt. %) and in Fig. 6.9 (8-16 wt. %) for AVR-asphaltenes in n-dodecane. At low concentrations, the scattering coefficients drop significantly in the temperature range of 120-150 ˚C, indicating that a major structural change occurs. From Table 6.3, the nature of the change is ambiguous. Bagheri et al [64] found liquid crystals in precipitated asphaltenes, and showed that Athabasca pentane-asphaltenes comprise at least two solid phases at room temperature (solid I and solid II). As temperature increases, solid I undergoes an endothermic transition to liquid which begins at room temperature. Solid II, on the other hand, undergoes an endothermic transition to liquid crystal at 65 ˚C, followed by an exothermic dissolution that ends at approximately 150 ˚C. After that temperature, asphaltenes are composed by two phases, solid I and liquid. These results were validated by experiments in hot-stage microscopy (HSM) as well as differential scanning calorimetry (DSC) [64]. Now with the advantage of scattering coefficient analysis, it can be affirmed that this transition also induces changes from a structural point of view. The disappearance of the liquid crystal phase in asphaltene aggregates leaves aggregates with a more open structure, consistent with a lower scattering coefficient. As temperature rises above 150 ˚C, the solid I phase in asphaltenes continue to transition to liquid. This, however, has little effect on the scattering coefficient value in n-dodecane. At higher asphaltene concentrations, Fig. 6.9, the impact of temperature on scattering

coefficient is more gradual but the transition to a lower scattering coefficient plateau is complete by 200 ˚C.

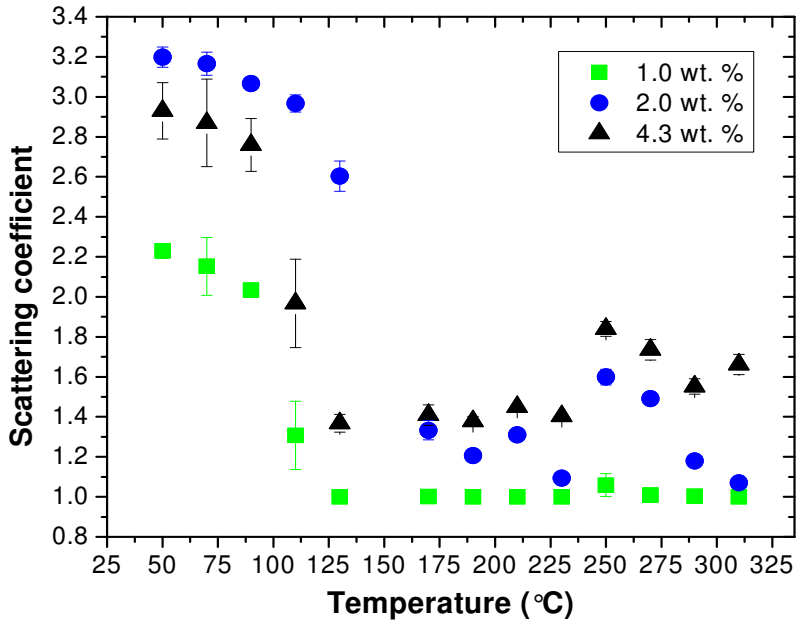

Figure 6.8. Scattering coefficients for the lower range of concentrations of AVR-asphaltenes in C-12

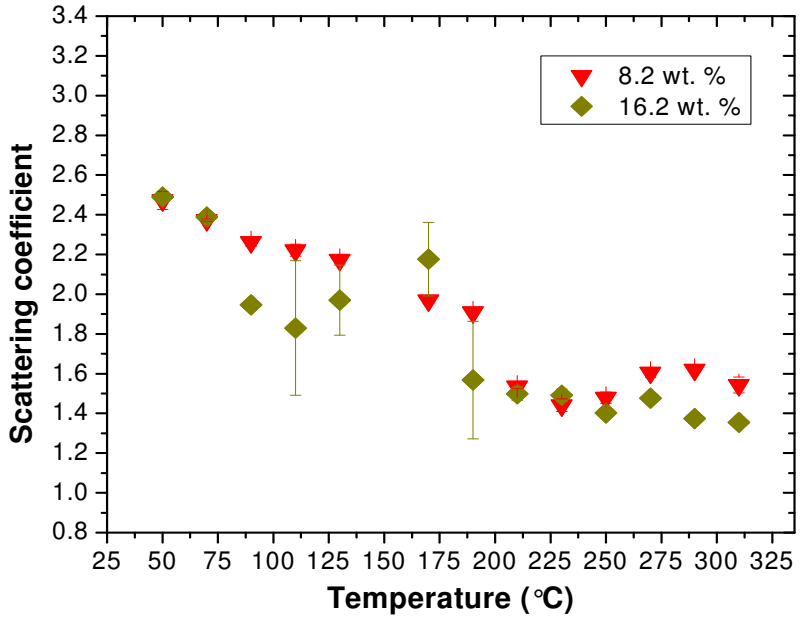

Figure 6.9. Scattering coefficients for the higher range of concentrations of AVR-asphaltenes in C-12

Scattering coefficients of AVR-asphaltenes in 1-methylnaphthalene, Fig. 6.10, display values within the range of 2.1-2.3, reflecting that even in chemically separated asphaltenes 1-methylnaphthalene does not promote disaggregation and the structure of the aggregates remain temperature and concentration invariant.

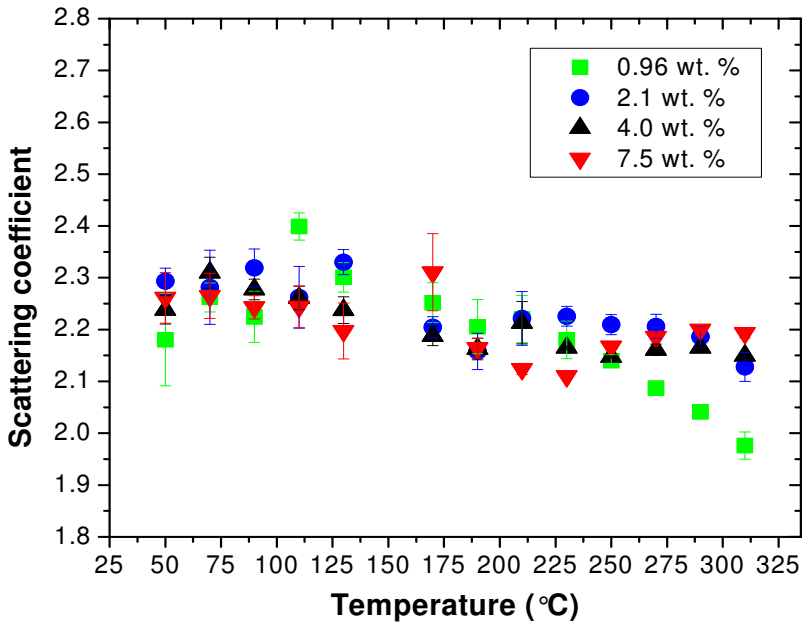

Figure 6.10. Scattering coefficients for AVR-asphaltenes in 1-methylnaphthalene

6.3.2.2. Scattering coefficients of bitumen permeate

Nanofiltered samples exhibit a very different behavior. Almost no changes are observed in the scattering coefficient values with temperature. This behavior, shown in Figure 6.11, is consistent with the radius of gyration values that are similarly temperature invariant. The temperature-averaged effect of diluent is summarized in Fig. 6.12. In 1-methylnaphthalene the aggregate structures possess a scattering coefficient of ~ 1.2, regardless of the asphaltene concentration. The scattering coefficient for AB-permeate is ~ 1.3, corresponding to a structure similar to the ones present on dilution in 1-methylnapthalene. In n-dodecane, the scattering coefficient is a function of dilution and reaches values greater than 2.

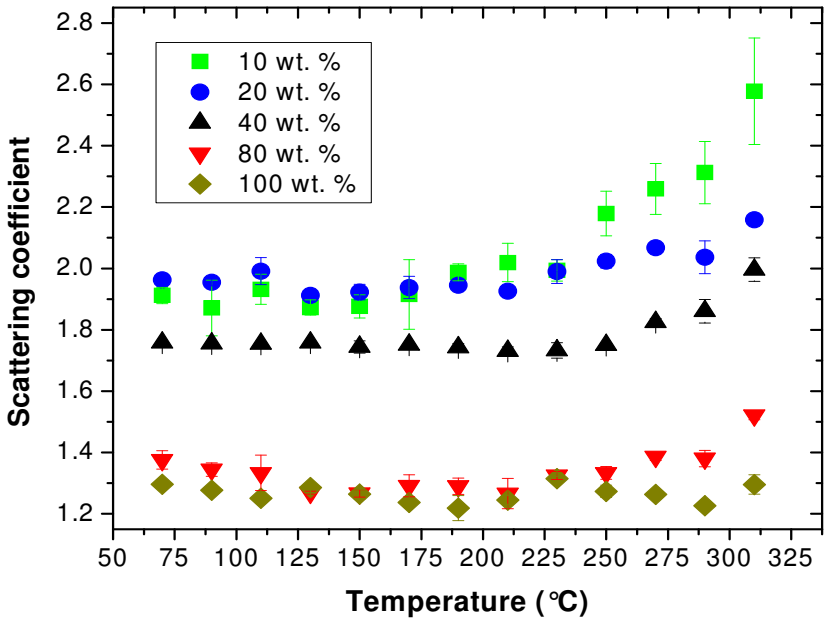

Figure 6.11. Scattering coefficients for AB-permeates in n-dodecane

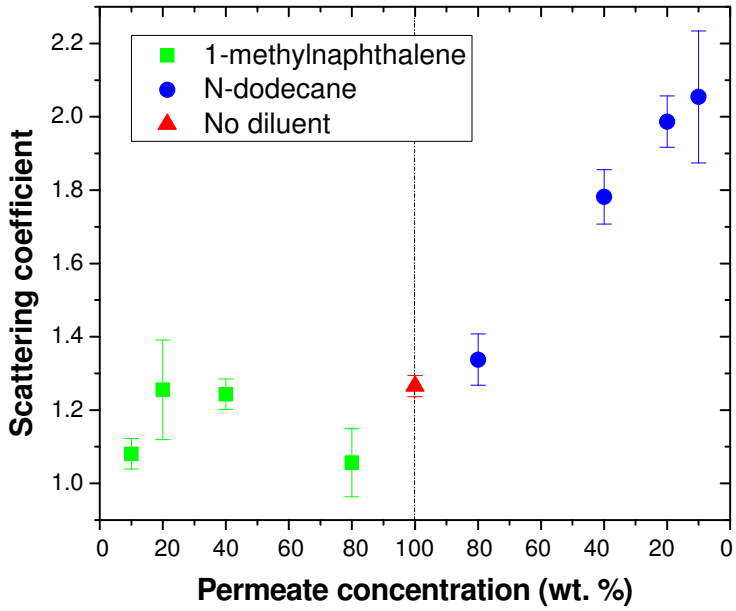

Figure 6.12. Effect of diluent in the scattering coefficients of AB-permeates

Tanaka et al. [26] suggested a hierarchy for asphaltene aggregates: *core aggregates*, formed by π-π stacking of asphaltene molecules and with a size of around 20 Å; *medium aggregates*, consisting of secondary aggregates formed from interactions with media and with a size range of 50-500 Å; and *fractal aggregates*, comprised by secondary aggregates that result from diffusion-limited cluster aggregation (DLCA)

or reaction-limited cluster aggregation (RLCA), independent of any media and with a size above 1000 Å. According to this hypothesis, physically separated asphaltene could be described as core asphaltene aggregates and only when in n-dodecane, as possibly medium aggregates (*see* Fig. 6.6). However, the larger aggregates present in n-dodecane have a larger scattering coefficient than the smaller ones in the permeate and the permeate diluted with 1-methylnaphthalene. This result is inconsistent with the notion of cluster growth where one would expect larger aggregates to be less structured and can only be explained if the dimensionality of the aggregates is changing e.g.: rods (scattering coefficient 1) forming clusters of rods (scattering coefficient ~ 2) .

In this context, valuable information can be extracted from SAXS measurements performed on AB-retentate + 1-methylnaphthalene. The asphaltene content in this sample was 56.7 wt. %. As the sample was retrieved from the upstream side of the filter, the sample is primarily filter cake, but also contains some unfiltered bitumen from the feed line. Consequently large as well as small asphaltene aggregates are expected to be present. Due to restricted access at the synchrotron facility, only one case was studied, namely, 10 wt. % AB-retentate in 1-methylnaphthalene. Fig. 6.13 presents intensity profiles for some of the data collected. The emissions only display power-law scattering, due to the large aggregates in the mixture. Again, based on the value of q_{min}, scatterers larger than 20 nm are anticipated. The scattering coefficients are presented in Fig. 6.14. The temperature invariant value is 3.2 – a much higher value than obtained for the nanofiltered asphaltene bitumen, 1.2 +/- 0.05 (Fig. 6.12) or the C5-asphaltene samples 2.2 +/- 0.1 (Fig. 6.10) in the same diluent. In fact, as the value exceeds 3, if only marginally, the scattering coefficient could be linked to a surface fractal for a fully dense object with a rough surface. One interpretation would be that these domains constitute bulk asphaltene rich phases that are unrelated to the dispersed structures in the other mixtures. Irrespective of their origin(s), structural differences are apparent and again the larger scatterers are more ordered than the smaller ones.

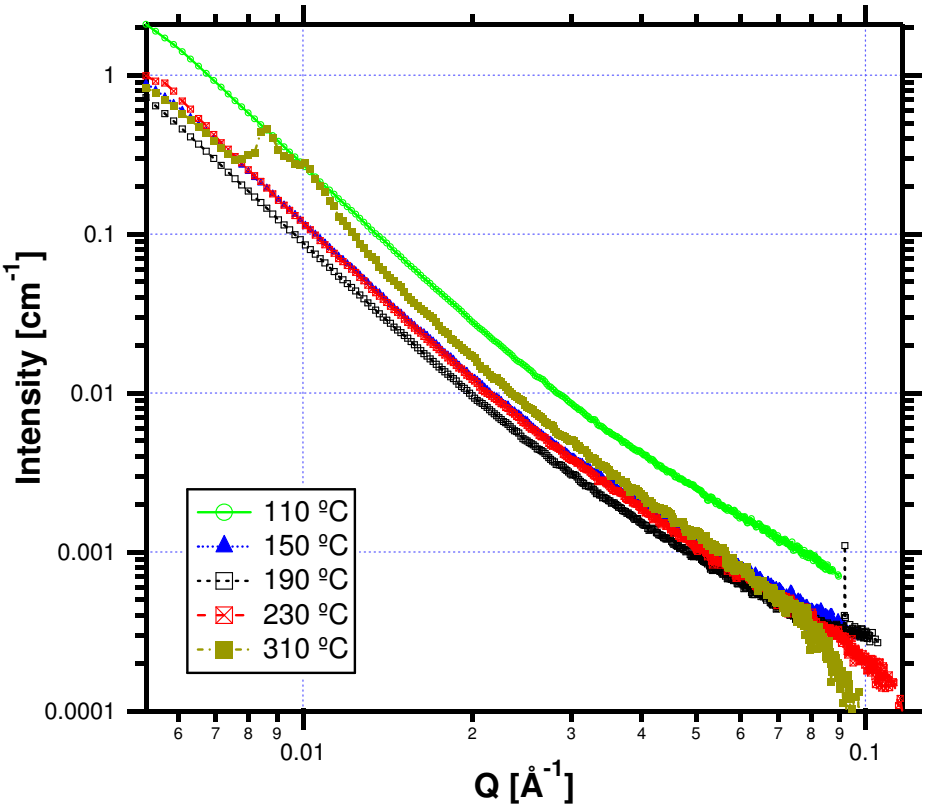

Figure 6.13. SAXS emission profiles of 10 wt. % AB-retentate (5.7 wt % asphaltenes) in 1-methylnaphthalene.

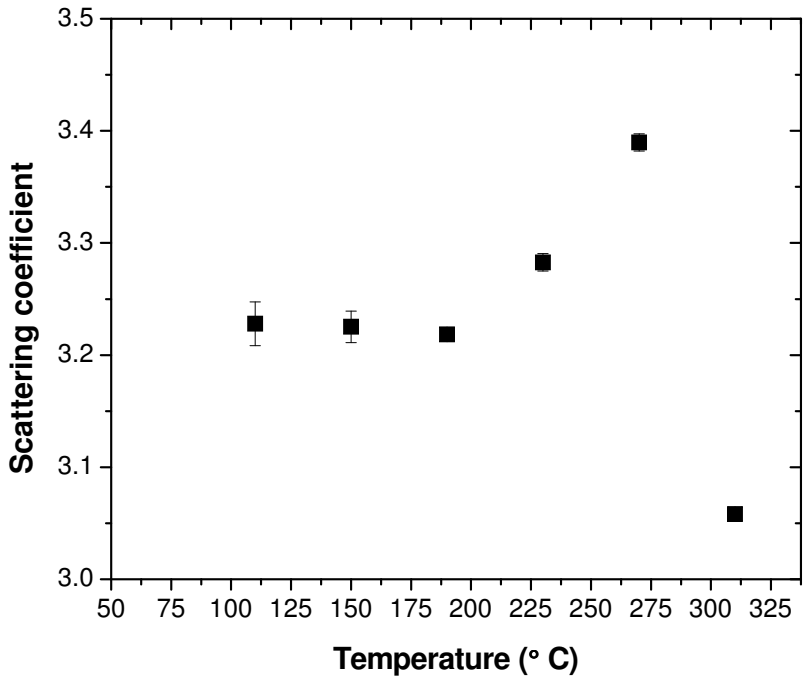

Figure 6.14. Scattering coefficients for AB-retentate (10wt %) in 1-methylnaphthalene.

6.3.2.3. Comparison of scattering coefficients in physically and chemically separated asphaltenes

The scattering coefficients for bitumen permeates diluted in n-dodecane are significantly lower at low temperature and significantly higher at high temperature when compared to chemically separated asphaltenes in dodecane as shown in Fig. 6.15 for 4 wt. % asphaltenes. The scattering coefficient for the diluted permeate is approximately 1.7 throughout the entire temperature range examined, while the value for pentane-asphaltenes drops from approximately 3.0 to 1.4 as temperature is raised above 100 ˚C. AVR-asphaltenes exhibit a structural transition from a dense three dimensional structure to a less ordered structure, neither the transition nor the start and end states arise in the permeate or diluted permeate.

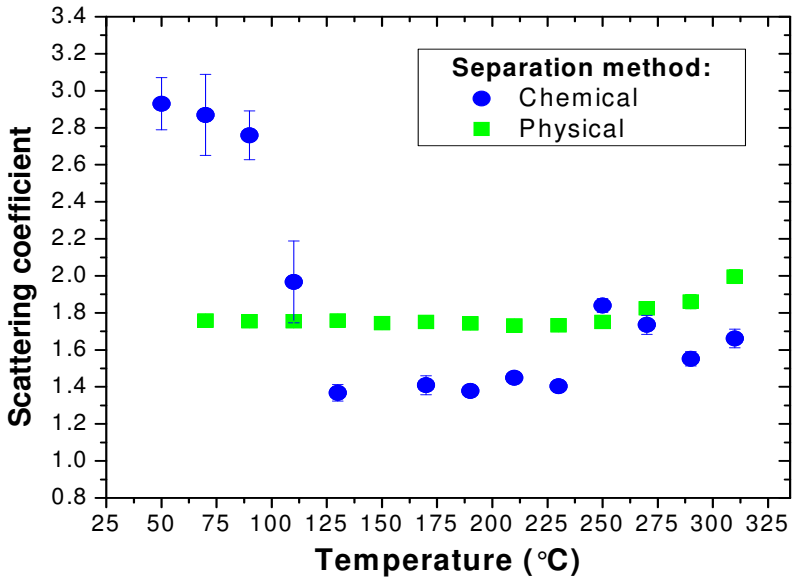

Figure 6.15. Scattering coefficients for 4 wt. % asphaltenes in n-dodecane

In 1-methylnphathalene, Fig. 6.16, the scatterer structures are temperature invariant. For diluted permeate the value is ~ 1.2 while for diluted asphaltenes the value is 2.2 for a net asphaltene concentration of 4 wt. %. Again the structures present differ significantly. The absence of a temperature dependence for the scattering coefficient is also consistent with prior findings showing that 1-methylnaphthalene acts as an asphaltene aggregation inhibitor and not as a dispersant [65]. It is also important to recognize that only a fraction of the

chemically separated asphaltenes is observed in the experiments and the comparisons between observations must be made with caution.

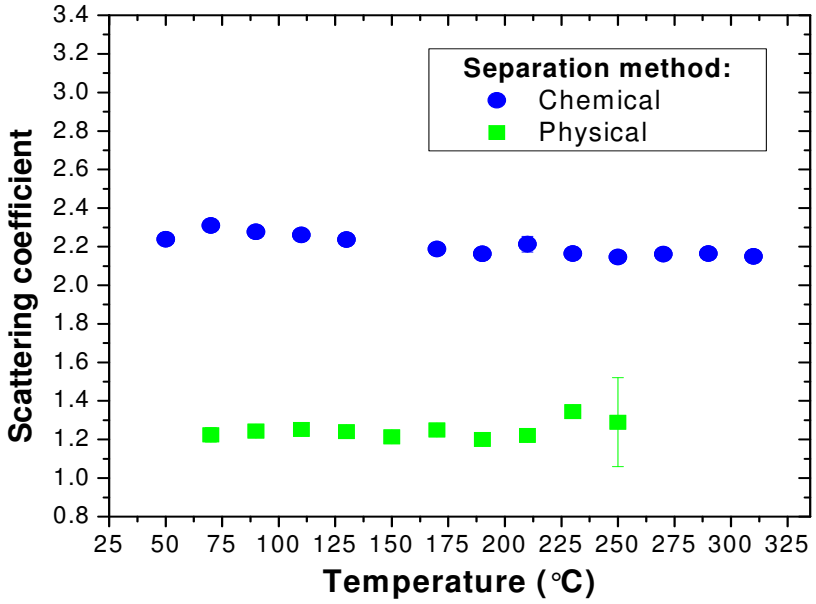

Figure 6.16. Scattering coefficients for 4 wt. % asphaltenes in 1-methylnaphthalene

6.4. Particle Size distribution analysis

Particle size distributions were assessed according to the method presented in section 4.3.3.2. The method was benchmarked using monodispersed silica nanospheres in water with reported nominal mean sizes. Fig. 6.17 exemplifies the particle size distribution results obtained. For a sample of 16 wt. % silica nanospheres, with nominal size of 20 nm, dispersed in water a Gaussian distribution with a mean radius of 23 nm and standard deviation of 5.2 nm was obtained. As no size distributions were supplied along with the silica solutions, a comparison of the polydispersity obtained is not feasible. However, it should be noted that nanoparticle samples are always expected to present some degree of polydispersity and number means are smaller than volume means. Here, number mean radii are presented along with the distribution widths to account for the possible polydispersity of the samples.

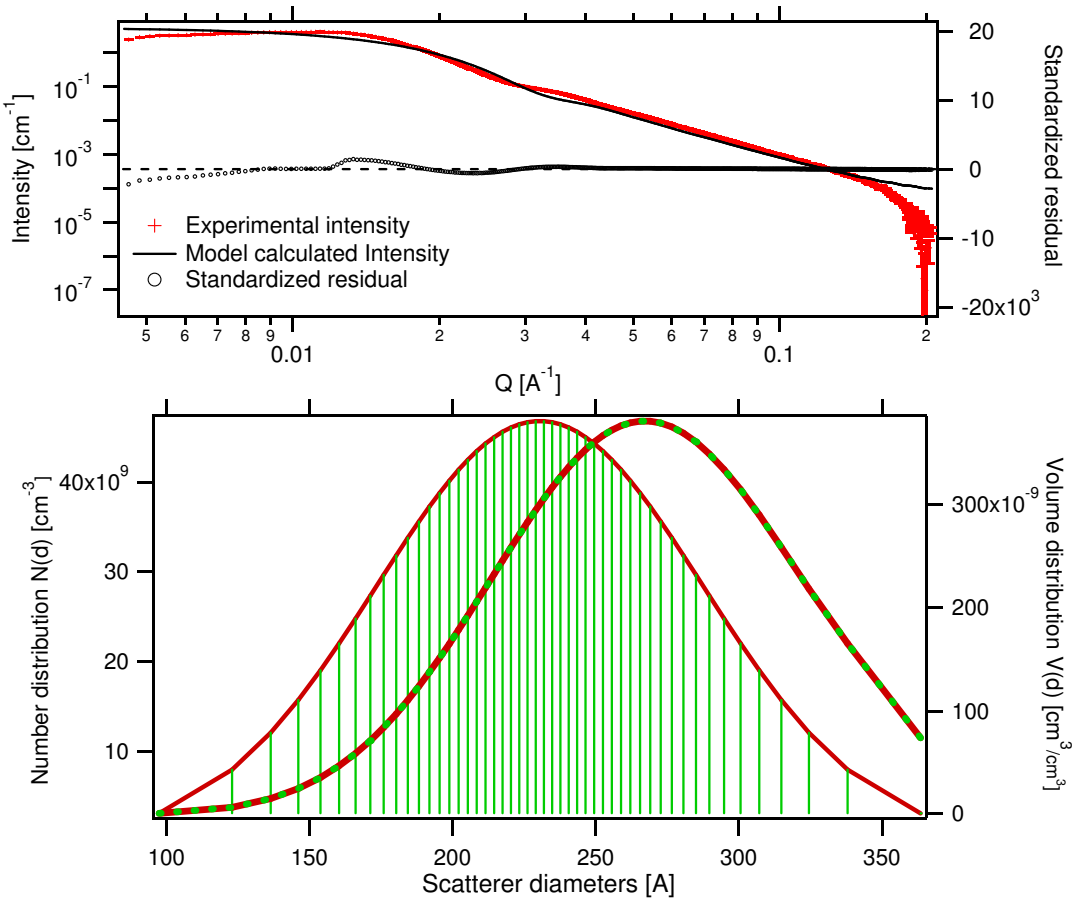

Figure 6.17. Particle size distribution estimation for a mixture of 16 wt. % silica nanospheres of nominal radius 20nm (exposure time: 0.05 s)

A parity plot for the average sizes obtained for the silica nanosphere samples using SAXS, for more than 200 samples, vs. the nominal size of the silica spheres is presented in Fig. 6.18. The SAXS particle size distribution estimations are in close agreement with the nominal size of the particles. Some scattering is observed, particularly for larger silica particles, as the width of the resulting distributions increased considerably. The success of these evaluations provides a solid reference point for evaluation of SAXS emission profiles from both physically and chemically separated asphaltenes, although it is not clear whether the properties of the aggregates permit such evaluation.

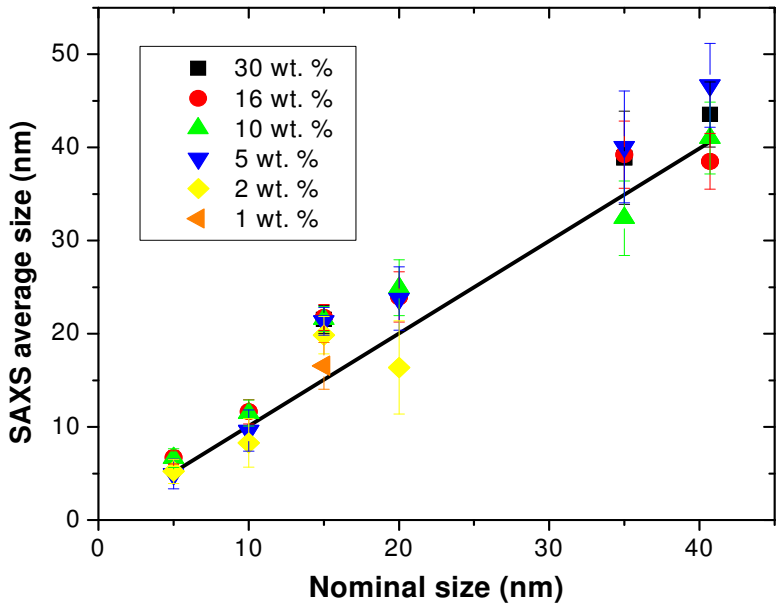

Figure 6.18. Comparison of PSD results with the silica spheres nominal sizes (exposure time: 0.1 s)

6.4.1. Chemically separated asphaltenes

Athabasca vacuum residue pentane-asphaltenes present a significant challenge for particle size distribution estimation. As explained in section 6.2, the SAXS emission profiles obtained for these samples do not possess low-q plateaus, which correspond to the average structural size according to Guinier's law. Therefore, direct size estimation in this case remains unfeasible. However, an approximate particle size range for these asphaltenes can be extracted from q-minimum values [3, 4]. Here, q_{min}^{-1} is the maximum particle size observable throughout the experimental window selected; consequently, the scatterers possess particle sizes larger than q_{min}^{-1}. Chemically separated asphaltenes include scatterers larger than 250 Å. Further details such as mean size and polydispersity, cannot be determined.

6.4.2. Physically separated asphaltenes

Particle size distribution calculations were succesfully performed on Athasbaca bitumen permeate samples. Several particle shapes such as spheres [35-37], thin disks, oblate cylinders [27, 40], and prolate ellipsoids [28, 31] have all been proposed for characterizing asphaltenes and asphaltene fractions. However, it has

been recently noted that small-angle scattering emission profiles tend to be featureless and significant differences in scatterer shape only induce subtle impacts in the resulting model intensity profiles [70]. In fact, Chodakowski showed that SAXS emission profiles from rosette nanotubes could be fitted as polydispersed spheres, where the distribution radius peak corresponded to the nanotube radius [70]. Based on this, asphaltene aggregates were assumed to be polydispersed hard spheres in the particle size distribution calculations. The values obtained must be considered tentative and relative in nature unless supported exogenously.

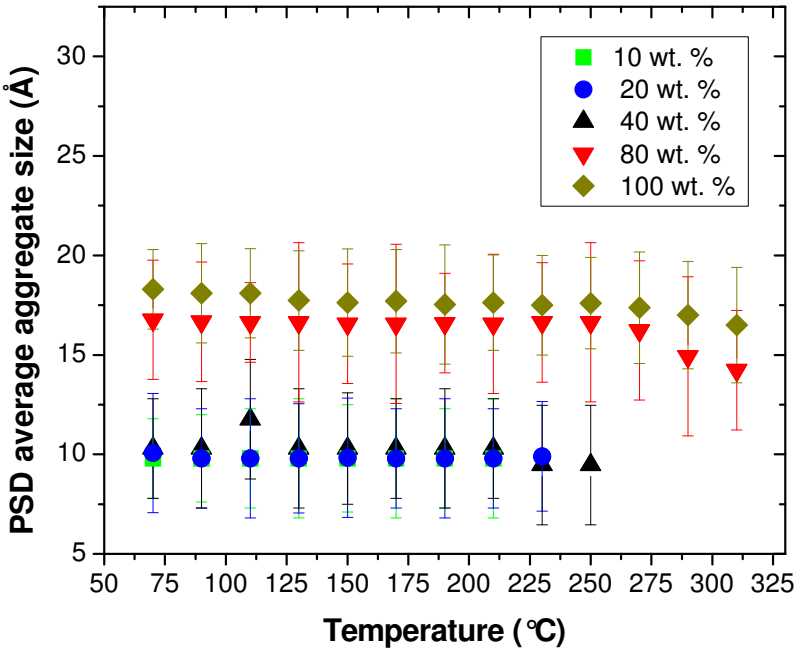

Figure 6.19. Distribution aggregate radii for Athabasca bitumen permeates (wt. %) in 1-MN

Figure 6.19 illustrates the results obtained from particle size distribution estimations on AB-permeates in 1-methylnaphthalene, with the error bars representing the half-height full-width of the distributions. Once again, the mean radius for each distribution is temperature invariant, reflecting the stability of the scatterers in the permeates. The values of the mean radii, falling in the 10-20 Å size range, also conform with those obtained from radius of gyration calculations, Fig. 6.22.

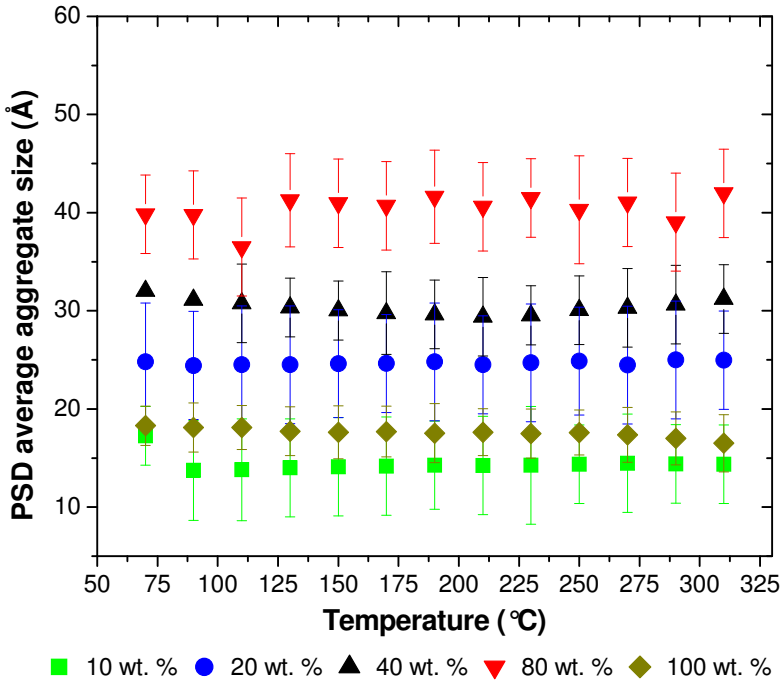

Figure 6.20. Distribution aggregate radii for Athabasca bitumen permeates (wt. %) in C-12

Fig. 6.20 summarizes the results obtained for AB-permeates in n-dodecane. Again, the scatterer size distributions are temperature invariant. Dilution of the permeate in n-dodecane appears to have an impact on the resulting average aggregate size. However, the values and trends diverge from those obtained from radii of gyration measurements, as observed in Fig. 6.21 and Fig. 6.22. This should only occur if the particles are asymmetric but may reflect other inappropriate assumptions required for model dependent fits to data. Allowing multiple particle distributions in the calculations had no effect in data reconciliation as they fell within the same size range. Changing the scatterer shape, however, had the most significant effect. It is important to note that multidimensional objects can only be fit to provide one of the dimensions forcing the assumption of the remaining geometric parameters. For algebraic rods, good fit in the SAXS emission profiles was found for rod lengths fixed to a size range of 50-60 Å, resulting in rod radii of 10-20 Å. Other scatterer shapes were tested but proved unsuccessful.

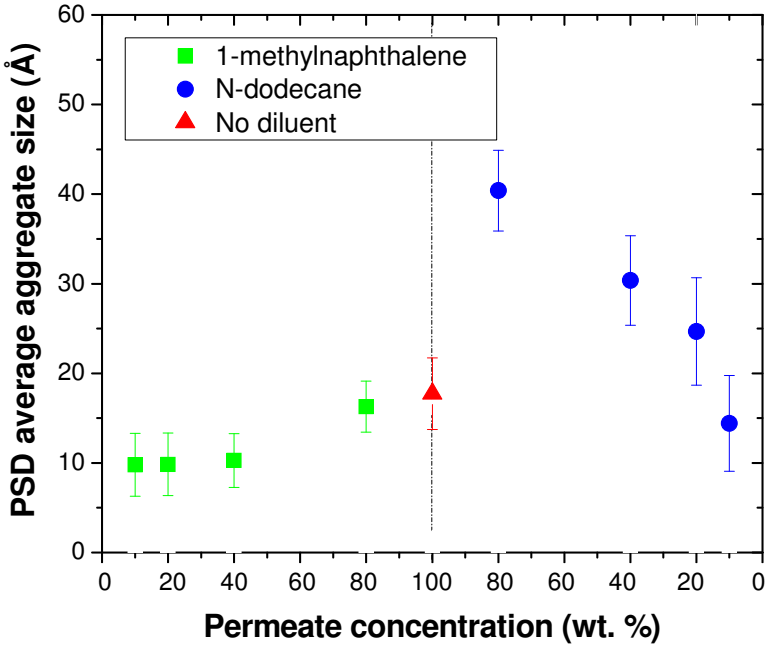

Figure 6.21. Effect of diluent in the SAXS-estimated particle size distributions of AB-permeate

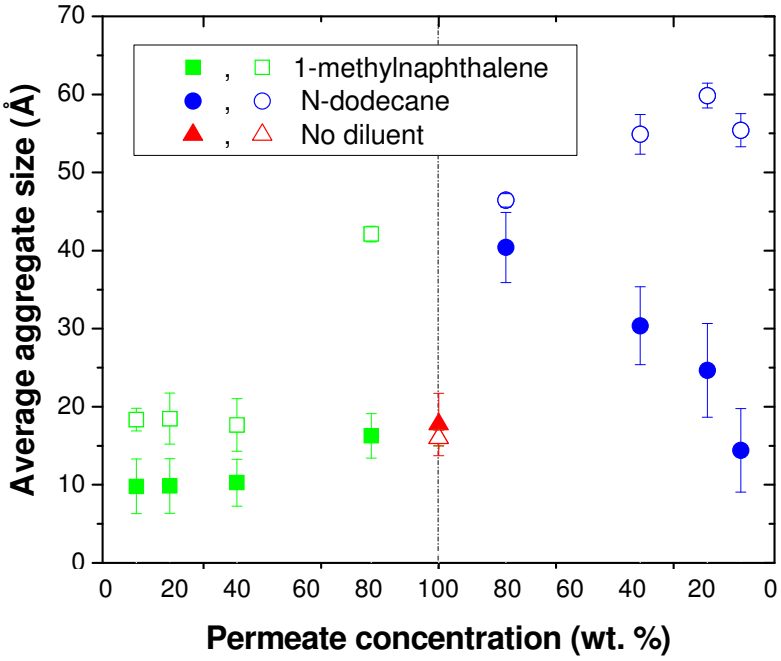

Figure 6.22. Size results of AB-permeates through unified modeling and particle size distribution estimations (*open symbols:* radii of gyration, *filled symbols:* Particle size distribution calculations)

Results from radius of gyration, scattering coefficient, and now particle size distributions, all seem to concur with the idea extracted from Stoyanov *et al.* [65] in which 1-methylnaphthalene was suggested to act as an aggregation inhibitor in asphaltenes while lacking the dispersant qualities of other aromatic materials such as toluene. This finding challenges a preconceived idea about asphaltenes in which aromatic materials dissolve asphaltene aggregates; factors like aromaticity but also atomic heterogeneity reinforce the dispersant capabilities of diluents toward asphaltene aggregation [65]. On the other hand, the effect of n-dodecane was clear since it promotes aggregation due to repulsive interactions. Assumptions made in model dependent analyses, however, need to be reassessed carefully to reconciliate results with model-independent analyses.

Finally, it is important to note that some authors have a very contrasting idea about asphaltenes that would compromise the results and purpose of this project and therefore, need to be addressed. Sirota [29, 71] through a series of small-angle neutron and X-ray scattering studies concluded that asphaltenes in diluents were comprised of highly viscous liquids that coexist in the vicinity of a glass-transition, for which any analysis considering asphaltenes as a particulate suspension system is fundamentally inaccurate. Multiple evidences can be used to challenge such affirmation. Zhao *et al.* [9], in a extensive study were able to filter out Maya and Athabasca asphaltenes from their native oils at 200 ˚C without the use of any chemicals, proving the particulate nature of the aggregates even at such high temperature. Bagheri *et al.* [64] in a very innovative study were capable of identify and visualize the presence of liquid crystals and solids in asphaltene samples through hot-stage microscopy (HSM) measurements. Other supporting evidence includes differential scanning calorimetry (DSC) and rheometric results [10, 57, 72].

Chapter VII
CONCLUSIONS AND FUTURE WORK

7.1. Conclusions

Multiple aspects of asphaltene properties and behavior remain unresolved. As noted in the literature review, experimental and theoretical results that contradict one another were found in almost every area addressed. This research attempted to explore the origins of the ambiguity and to provide a better understanding about some physical features of asphaltene aggregates such as aggregate size and structure. Small-angle X-ray scattering analyses were performed to determine how these properties change with extraction and experimental conditions and attempts were made to link observations to recent phase behavior and rheological measurements for related samples.

AVR pentane-asphaltenes and Athabasca Bitumen retentate displayed power-law scattering in the entire q-range studied, indicating the presence of large aggregates that are not observable in the experimental window of the measurements. Values of q_{min} indicate the presence of aggregates larger than 250 Å in AVR-asphaltenes when diluted in either n-dodecane or 1-methylnaphthalene while for Athabasca Bitumen retentate, aggregates larger than 200 Å were present on dilution in 1-methylnaphthalene. Only the properties of smaller aggregates in these mixtures are observed in the SAXS measurements reported here.

Changes in scattering coefficient values with temperature suggest that AVR asphaltene aggregates undergo a significant structural transition when diluted in n-dodecane. The temperature of the transition is composition dependent but falls in the range 110-200 °C. This transition is consistent with calorimetric, rheologic and cross polarized light microscopy results for neat asphaltenes, which undergo a complex sequence of phase transitions from solid to liquid that include this temperature range.

On dilution in 1-methylnaphthalene AVR asphaltenes possess a different structure at room temperature than in n-dodecane, and the structure is both composition and temperature invariant. This result may be linked to the dissolution of the liquid crystal phase present in asphaltenes on exposure to this diluent, as observed with cross polarized light microscopy in toluene [73].

By contrast, more than 60 % of scatterers by weight present in Athabasca bitumen passed through a 200 Å filter. Scatterers in nanofiltered and diluted nanofiltered bitumen samples were small, based on radii of gyration measurements, compared with the filter size and with AVR asphaltenes. They also presented temperature invariant structural parameters which differed from AVR-asphaltenes, and diluted retentate samples. On dilution in 1-methylnaphthalene, radii of gyration were in the range of 15-20 Å and the scattering coefficients were $\sim$ 1.2. On dilution in n-dodecane, radii of gyration and scattering coefficient values increased with dodecane concentration to $\sim$ 60 Å and $\sim$ 2, respectively.

The asphaltenes present in the retentate possessed a temperature invariant scattering coefficient (3.2) that was significantly larger than the temperature and composition invariant scattering coefficients for AVR asphaltenes (2.1) and asphaltenes present in the permeate (1.2).

The values of the scattering coefficients for both AVR asphaltenes and for scatters in Athabasca bitumen range from 1 to 3. The broad range of values and properties implied for these closely related samples was unexpected. The values are subject to multiple interpretations and provide little direct information concerning structure in the absence of exogenous and independent structure or phase behavior data.

Application of model dependent analysis to the scatterers in Athabasca bitumen permeates suggests that in the bitumen and on dilution in 1-methylnaphthalene, the scatterers are globular in nature as the radii of gyration and the spherical model dependent diameters are similar and possess the same trends with composition. By contrast, on dilution in n-dodecane, the two sets of nominal leading dimensions diverge. Either the nominal shape is not globular or other assumptions in the model are not valid.

7.2. Recommendations and future work

Direct use of small-angle X-ray scattering proved to be a limited technique for the physical characterization of asphaltenes. Future work on this topic should take advantage of contrast variation methods available in SANS or SAXS in order to understand the influence of the diluent electron density in the resulting emission profiles. This study also reinforces the need to extend the q-range for the intensity profiles associated with chemically separated asphaltenes. This could be achieved by performing complementing measurements on ultra or very small-angle X-ray scattering (USAXS or V-SAXS), as performed by Barré's group at IFP. Significant experimental challenges are involved if this avenue is to be pursued. It is not clear that this would be the most productive line of inquiry given the gulf between the properties of scatterers in bitumen and those of chemically separated AVR asphaltenes, with an essentially identical chemical composition. Research targeting a more complete understanding of the properties of scatterers in fluids of industrial interest or physically separated fractions is a preferred line of inquiry for applied research where the understanding and improvement of industrial processes is a primary goal.

Other related lines of inquiry include examination of rheological and calorimetric properties of retentate, asphaltene and permeate samples with the objective of identifying and further integrating SAXS data with other types of observations related to the structure and phase behaviour of asphaltenes.

REFERENCES

1. Chang, C.-L. and H.S. Fogler, *Stabilization of Asphaltenes in Aliphatic Solvents Using Alkylbenzene-Derived Amphiphiles. 1. Effect of the Chemical Structure of Amphiphiles on Asphaltene Stabilization.* Langmuir, 1994. 10(6): p. 1749-1757.
2. Speight, J.G., *Les Asphaltènes, Composés Pétroliers - Partie 2 : L'effet Des Asphaltènes Et Des Résines Sur Les Procédés De Récupération Et De Raffinage.* Oil & Gas Science and Technology - Rev. IFP, 2004. 59(5): p. 479-488.
3. Savvidis, T.G., D. Fenistein, L. Barré, and E. Behar, *Aggregated Structure of Flocculated Asphaltenes.* American Institute of Chemical Engineers. AIChE Journal, 2001. 47(1): p. 206-211.
4. Gawrys, K.L., P.M. Spiecker, and P.K. Kilpatrick, *The Role of Asphaltene Solubility and Chemical Composition on Asphaltene Aggregation.* Petroleum Science and Technology, 2003. 21(3): p. 461 - 489.
5. Fenistein, D., L. Barré, D. Broseta, D. Espinat, A. Livet, J.-N. Roux, and M. Scarsella, *Viscosimetric and Neutron Scattering Study of Asphaltene Aggregates in Mixed Toluene/Heptane Solvents.* Langmuir, 1998. 14(5): p. 1013-1020.
6. Fenistein, D. and L. Barré, *Experimental Measurement of the Mass Distribution of Petroleum Asphaltene Aggregates Using Ultracentrifugation and Small-Angle X-Ray Scattering.* Fuel, 2001. 80(2): p. 283-287.
7. Jestin, J. and L. Barré, *Application of NMR Solvent Relaxation and SAXS to Asphaltenes Solutions Characterization.* Journal of Dispersion Science & Technology, 2004. 25(3): p. 341-347.
8. Zhao, B., M. Becerra, and J.M. Shaw, *On Asphaltene and Resin Association in Athabasca Bitumen and Maya Crude Oil.* Energy & Fuels, 2009. 23(9): p. 4431-4437.
9. Zhao, B. and J.M. Shaw, *Composition and Size Distribution of Coherent Nanostructures in Athabasca Bitumen and Maya Crude Oil.* Energy & Fuels, 2007. 21(5): p. 2795-2804.
10. Hasan, M.D.A., M. Fulem, A. Bazyleva, and J.M. Shaw, *Rheological Properties of Nanofiltered Athabasca Bitumen and Maya Crude Oil.* Energy & Fuels, 2009. 23(10): p. 5012-5021.
11. Sheu, E.Y., *Small Angle Scattering and Asphaltenes.* Journal of Physics: Condensed Matter, 2006. 18(36): p. S2485-S2498.
12. Mullins, O.C., *Petroleomics and Structure - Function Relations of Crude Oils and Asphaltenes*, in *Asphaltenes, Heavy Oils, and Petroleomics*, O.C. Mullins, E.Y. Sheu, A. Hammami, and A.G. Marshall, Editors. 2007, Springer: New York. p. 1-16.
13. Sheremata, J.M., M.R. Gray, H.D. Dettman, and W.C. McCaffrey, *Quantitative Molecular Representation and Sequential Optimization of Athabasca Asphaltenes.* Energy & Fuels, 2004. 18(5): p. 1377-1384.
14. Yarranton, H.W., *Asphaltene Self-Association.* Journal of Dispersion Science & Technology, 2005. 26(1): p. 5-8.
15. Cunico, R.L., E.Y. Sheu, and O.C. Mullins, *Molecular Weight Measurement of UG8 Asphaltene Using APCI Mass Spectroscopy.* Petroleum Science & Technology, 2004. 22(7/8): p. 787-798.
16. Groenzin, H. and O.C. Mullins, *Asphaltene Molecular Size and Weight by Time-Resolved Fluorescence Depolarization*, in *Asphaltenes, Heavy Oils, and*

Petroleomics, O.C. Mullins, E.Y. Sheu, A. Hammami, and A.G. Marshall, Editors. 2007, Springer: New York. p. 17-62.
17. Badre, S., C. Carla Goncalves, K. Norinaga, G. Gustavson, and O.C. Mullins, *Molecular Size and Weight of Asphaltene and Asphaltene Solubility Fractions from Coals, Crude Oils and Bitumen.* Fuel, 2006. 85(1): p. 1-11.
18. Buch, L., H. Groenzin, E. Buenrostro-González, S.I. Andersen, C. Lira-Galeana, and O.C. Mullins, *Molecular Size of Asphaltene Fractions Obtained from Residuum Hydrotreatment.* Fuel, 2003. 82(9): p. 1075-1084.
19. Morgan, T.J., M. Millan, M. Behrouzi, A.A. Herod, and R. Kandiyoti, *On the Limitations of UV/Fluorescence Spectroscopy in the Detection of High-Mass Hydrocarbon Molecules.* Energy & Fuels, 2004. 19(1): p. 164-169.
20. Boek, E.S., D.S. Yakovlev, and T.F. Headen, *Quantitative Molecular Representation of Asphaltenes and Molecular Dynamics Simulation of Their Aggregation.* Energy & Fuels, 2009. 23(3): p. 1209-1219.
21. Zhao, S., L.S. Kotlyar, J.R. Woods, B.D. Sparks, and K.H. Chung, *Effect of Thermal and Hydro-Catalytic Treatment on the Molecular Chemistry of Narrow Fractions of Athabasca Bitumen Pitch.* Energy & Fuels, 2000. 15(1): p. 113-119.
22. Obiosa-Maife, C., *Prediction of the Molecular Structure of Ill-Defined Hydrocarbons Using Vibrational ^{1}H and ^{13}C NMR Spectroscopy*, in *Chemical and Materials Engineering*. 2009, University of Alberta: Edmonton. p. 100.
23. Sheu, E.Y., *Petroleomics and Characterization of Asphaltene Aggregates Using Small-Angle Scattering*, in *Asphaltenes, Heavy Oils, and Petroleomics*, O.C. Mullins, E.Y. Sheu, A. Hammami, and A.G. Marshall, Editors. 2007, Springer: New York. p. 353-374.
24. Rastegari, K., W.Y. Svrcek, and H.W. Yarranton, *Kinetics of Asphaltene Flocculation.* Industrial & Engineering Chemistry Research, 2004. 43(21): p. 6861-6870.
25. Hung, J., J. Castillo, and A. Reyes, *Kinetics of Asphaltene Aggregation in Toluene/Heptane Mixtures Studied by Confocal Microscopy.* Energy & Fuels, 2005. 19(3): p. 898-904.
26. Tanaka, R., E. Sato, J.E. Hunt, R.E. Winans, S. Sato, and T. Takanohashi, *Characterization of Asphaltene Aggregates Using X-Ray Diffraction and Small-Angle X-Ray Scattering.* Energy & Fuels, 2004. 18(4): p. 1118-1125.
27. Gawrys, K.L. and P.K. Kilpatrick, *Asphaltenic Aggregates Are Polydisperse Oblate Cylinders.* Journal of Colloid and Interface Science, 2005. 288(2): p. 325-334.
28. Tanaka, R., J.E. Hunt, R.E. Winans, P. Thiyagarajan, S. Sato, and T. Takanohashi, *Aggregates Structure Analysis of Petroleum Asphaltenes with Small-Angle Neutron Scattering.* Energy & Fuels, 2002. 17(1): p. 127-134.
29. Sirota, E.B., *Physical Structure of Asphaltenes.* Energy & Fuels, 2005. 19(4): p. 1290-1296.
30. Rahmani, N.H.G., T. Dabros, and J.H. Masliyah, *Fractal Structure of Asphaltene Aggregates.* Journal of Colloid and Interface Science, 2005. 285(2): p. 599-608.
31. Tanaka, R., J.E. Hunt, R.E. Winans, P. Thiyagarajan, S. Sato, and T. Takanohashi, *Aggregates Structure Analysis of Petroleum Asphaltenes with Small-Angle Neutron Scattering.* Energy & Fuels, 2003. 17(1): p. 127-134.
32. Rahmani, N.H.G., T. Dabros, and J.H. Masliyah, *Evolution of Asphaltene Floc Size Distribution in Organic Solvents under Shear.* Chemical Engineering Science, 2004. 59(3): p. 685-697.

33. Maham, Y., M.G. Chodakowski, X. Zhang, and J.M. Shaw, *Asphaltene Phase Behavior: Prediction at a Crossroads.* Fluid Phase Equilibria, 2005. 227(2): p. 177-182.
34. Headen, T.F., E.S. Boek, J.r. Stellbrink, and U.M. Scheven, *Small Angle Neutron Scattering (SANS and V-SANS) Study of Asphaltene Aggregates in Crude Oil.* Langmuir, 2008. 25(1): p. 422-428.
35. Barré, L., S. Simon, and T. Palermo, *Solution Properties of Asphaltenes.* Langmuir, 2008. 24(8): p. 3709-3717.
36. Xu, Y., Y. Koga, and O.P. Strausz, *Characterization of Athabasca Asphaltenes by Small-Angle X-Ray Scattering.* Fuel, 1995. 74(7): p. 960-964.
37. Evdokimov, I.N., Eliseev, and B.R. Akhmetov, *Assembly of Asphaltene Molecular Aggregates as Studied by near-UV/Visible Spectroscopy: I. Structure of the Absorbance Spectrum.* Journal of Petroleum Science and Engineering, 2003. 37(3-4): p. 135-143.
38. Da Silva, S.M.C. and K. Rajagopal, *Steady State Size Distribution of Asphaltenes by Flocculation from Toluene/n-Heptane Mixtures.* Petroleum Science & Technology, 2004. 22(7/8): p. 1073-1085.
39. Bearsley, S., A. Forbes, and R.G. Haverkamp, *Direct Observation of the Asphaltene Structure in Paving-Grade Bitumen Using Confocal Laser-Scanning Microscopy.* Journal of Microscopy, 2004. 215(2): p. 149-155.
40. Gawrys, K.L., G.A. Blankenship, and P.K. Kilpatrick, *Solvent Entrainment in and Flocculation of Asphaltenic Aggregates Probed by Small-Angle Neutron Scattering.* Langmuir, 2006. 22(10): p. 4487-4497.
41. Svergun, D.I. and M.H.J. Koch, *Small-Angle Scattering Studies of Biological Macromolecules in Solution.* Reports on Progress in Physics, 2003. 66(10): p. 1735-1782.
42. Perkins, S.J., *X-Ray and Neutron Solution Scattering*, in *Modern Physical Methods in Biochemistry Part B*, A. Neuberger and L.L.M.V. Deenen, Editors. 1988, Elsevier: Amsterdam. p. 143-265.
43. Narayanan, T., *Synchrotron Small-Angle X-Ray Scattering*, in *Soft-Matter Characterization*, R. Borsali and R. Pecora, Editors. 2008, Springer: New York. p. 899-952.
44. Feigin, L.A. and D.I. Svergun, *Structure Analysis by Small-Angle X-Ray and Neutron Scattering*, ed. G.W. Taylor. 1987, New York: Plenum Press. 335.
45. Guinier, A. and D.L. Dexter, *X-Ray Studies of Materials*. 1963, New York: Interscience Publishers. 153.
46. Guinier, A. and G. Fournet, *Small-Angle Scattering of X-Rays*. 1955, New York: John Wiley & Sons. 259.
47. Glatter, O. and O. Kratky, *Small-Angle X-Ray Scattering*. 1982, New York: Academic Press Inc. 511.
48. *The Scanning Probe Image Processor SPIP™ Version 4.8 - User's and Reference Guide*. 2008, Image Metrology A/S: Hørsholm, Denmark.
49. *Igor Pro Version 6.0 - Getting Started*. 2007, WaveMetrics, Inc.
50. Ilavsky, J., P.R. Jemian, A.J. Allen, G. Beaucage, and A. Nelson, *Irena SAS Modeling Macros - Version 2.27*. 2008.
51. Ilavsky, J. and P.R. Jemian, *Irena: Tool Suite for Modeling and Analysis of Small-Angle Scattering*. Journal of Applied Crystallography, 2009. 42(2): p. 347-353.

52. Lake, J.A., *An Iterative Method of Slit-Correcting Small-Angle X-Ray Data.* Acta Crystallographica, 1967. 23: p. 191-194.
53. Jemian, P.R., *Characterization of Steels by Anomalous Small-Angle X-Ray Scattering*. 1990.
54. Beaucage, G., S. Rane, S. Sukumaran, M.M. Satkowski, I.A. Schechtman, and Y. Doi, *Persistence Length of Isotactic Poly(Hydroxy Butyrate).* Macromolecules, 1997. 30: p. 4158-4162.
55. Beaucage, G., *Approximations Leading to a Unified Exponential / Power-Law Approach to Small-Angle Scattering.* Journal of Applied Crystallography, 1995. 28(6): p. 717-728.
56. Beaucage, G., *Small-Angle Scattering from Polymeric Mass Fractals of Arbitrary Mass-Fractal Dimension.* Journal of Applied Crystallography, 1996. 29(2): p. 134-146.
57. Fulem, M., M. Becerra, M.D.A. Hasan, B. Zhao, and J.M. Shaw, *Phase Behaviour of Maya Crude Oil Based on Calorimetry and Rheometry.* Fluid Phase Equilibria, 2008. 272(1-2): p. 32-41.
58. Shenoy, G.K. and D.E. Moncton, *An Overview of the Advanced Photon Source.* Nuclear Instruments and Methods in Physics Research Section A: Accelerators, Spectrometers, Detectors and Associated Equipment, 1988. 266(1-3): p. 38-43.
59. Mills, D.M., *The Advanced Photon Source: A Status Report.* Nuclear Instruments and Methods in Physics Research Section A: Accelerators, Spectrometers, Detectors and Associated Equipment, 1992. 319(1-3): p. 33-39.
60. Beno, M.A., G. Jennings, M. Engbretson, G.S. Knapp, C. Kurtz, B. Zabransky, J. Linton, S. Seifert, C. Wiley, and P.A. Montano, *Basic Energy Sciences Synchrotron Radiation Center Undulator Sector at the Advanced Photon Source.* Nuclear Instruments and Methods in Physics Research Section A: Accelerators, Spectrometers, Detectors and Associated Equipment, 2001. 467-468(Part 1): p. 690-693.
61. Xiaohui, Z., M. Chodakowski, and J.M. Shaw, *Dynamic Interfacial Zone and Local Phase Concentration Measurements in Emulsions, Dispersions, and Slurries.* Journal of Dispersion Science & Technology, 2004. 25(3): p. 277-285.
62. Gray, M.R. and J.H. Masliyah, *Extraction and Upgrading of Oilsands Bitumen - Intensive Short Course*. 2006, University of Alberta: Edmonton.
63. Carnahan, N.F., L. Quintero, D.M. Pfund, J.L. Fulton, R.D. Smith, M. Capel, and K. Leontaritis, *A Small Angle X-Ray Scattering Study of the Effect of Pressure on the Aggregation of Asphaltene Fractions in Petroleum Fluids under near-Critical Solvent Conditions.* Langmuir, 1993. 9(8): p. 2035-2044.
64. Bagheri, S.R., A. Bazyleva, M.R. Gray, W.C. McCaffrey, and J.M. Shaw, *Observation of Liquid Crystals in Heavy Petroleum Fractions.* Energy & Fuels, 2010. 24(8): p. 4327–4332.
65. Stoyanov, S.R., S. Gusarov, and A. Kovalenko, *Multiscale Modelling of Asphaltene Disaggregation.* Molecular Simulation, 2008. 34(10): p. 953 - 960.
66. Takanohashi, T., S. Sato, and R. Tanaka, *Structural Relaxation Behaviors of Three Different Asphaltenes Using MD Calculations.* Petroleum Science & Technology, 2004. 22(7/8): p. 901-914.
67. Chianelli, R.R., M. Siadati, A. Mehta, J. Pople, L.C. Ortega, and L.Y. Chiang, *Self-Assembly of Asphaltene Aggregates: Synchrotron, Simulation and Chemical Modelling Techniques Applied to Problems in the Structure and Reactivity of*

Asphaltenes, in *Asphaltenes, Heavy Oils, and Petroleomics*, O.C. Mullins, E.Y. Sheu, A. Hammami, and A.G. Marshall, Editors. 2007, Springer: New York. p. 375-400.
68. Dabir, B., M. Nematy, A.R. Mehrabi, H. Rassamdana, and M. Sahimi, *Asphalt Flocculation and Deposition. Iii. The Molecular Weight Distribution.* Fuel, 1996. 75(14): p. 1633-1645.
69. Kolb, M. and H.J. Herrmann, *Surface Fractals in Irreversible Aggregation.* Physical Review Letters, 1987. 59(4): p. 454.
70. Chodakowski, M. and B. Zhao, *Interpretation of Small-Angle X-Ray Scattering Data*, in *Petroleum Thermodynamics Research Chair Advisory Commitee Meeting*. 2006, University of Alberta: Edmonton.
71. Sirota, E.B. and M.Y. Lin, *Physical Behavior of Asphaltenes.* Energy & Fuels, 2007. 21(5): p. 2809-2815.
72. Bazyleva, A.B., M.D.A. Hasan, M. Fulem, M. Becerra, and J.M. Shaw, *Bitumen and Heavy Oil Rheological Properties: Reconciliation with Viscosity Measurements.* Journal of Chemical & Engineering Data, 2009.
73. Bagheri, S.R., *PhD. Thesis*, in *Chemical and Materials Engineering*. 2007, University of Alberta: Edmonton (in progress).